

AD-A065 116

MASSACHUSETTS INST OF TECH LEXINGTON LINCOLN LAB
SOLID STATE RESEARCH, 1978:3.(U)
AUG 78 A L MCWHORTER

F/G 20/12

UNCLASSIFIED

ESD-TR-78-245

F1962R-78-C-0002
NL

1 OF 1
AD
A065116



END
DATE
FILMED
4 -79
DDC

ADA065116

DDC FILE COPY

12
Lee 1473
LEVEL II

3

Solid State Research

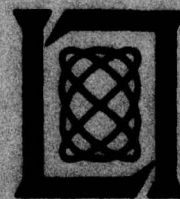
1978

Prepared
under Electronic Systems Division Contract F19628-78-C-0002 by

Lincoln Laboratory

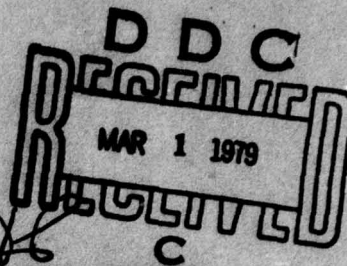
MASSACHUSETTS INSTITUTE OF TECHNOLOGY

LEXINGTON, MASSACHUSETTS



Approved for public release; distribution unlimited.

79 02 26 078



The work reported in this document was performed at Lincoln Laboratory, a center for research operated by Massachusetts Institute of Technology, with the support of the Department of the Air Force under Contract F19628-78-C-0002.

This report may be reproduced to satisfy needs of U.S. Government agencies.

The views and conclusions contained in this document are those of the contractor and should not be interpreted as necessarily representing the official policies, either expressed or implied, of the United States Government.

This technical report has been reviewed and is approved for publication.

FOR THE COMMANDER

Raymond L. Loiselle

Raymond L. Loiselle, Lt. Col., USAF
Chief, ESD Lincoln Laboratory Project Office

Non-Lincoln Recipients

PLEASE DO NOT RETURN

Permission is given to destroy this document
when it is no longer needed.

MASSACHUSETTS INSTITUTE OF TECHNOLOGY
LINCOLN LABORATORY

SOLID STATE RESEARCH

QUARTERLY TECHNICAL SUMMARY REPORT

1 MAY - 31 JULY 1978

ISSUED 17 NOVEMBER 1978

Approved for public release; distribution unlimited.

LEXINGTON

79 02 26 078

MASSACHUSETTS

ABSTRACT

This report covers in detail the solid state research work of the Solid State Division at Lincoln Laboratory for the period 1 May through 31 July 1978. The topics covered are Solid State Device Research, Quantum Electronics, Materials Research, Microelectronics, and Surface-Wave Technology. Funding is primarily provided by the Air Force, with additional support provided by the Army, ARPA, NSF, and DOE.

ACCESS FOR:		
NTIS	Air Section	<input checked="" type="checkbox"/>
DDC	Staff Section	<input type="checkbox"/>
UNANNOUNCED		<input type="checkbox"/>
JUSTIFICATION		
BY		
DISTRIBUTION/AVAILABILITY CODES		
Dist.	Special	SPECIAL
A		

CONTENTS

Abstract	iii
Introduction	vii
Reports on Solid State Research	xi
Organization	xvii
 I. SOLID STATE DEVICE RESEARCH	 1
A. 12-Element HgCdTe Photodiode Arrays	1
B. Effect of H ₂ on Residual Impurities in GaAs MBE Layers	3
 II. QUANTUM ELECTRONICS	 7
A. Tunable Ni:MgF ₂ Laser	7
B. Lasing and Fluorescence in K ₅ NdLi ₂ F ₁₀	9
C. Efficient, Two-Step Frequency Tripling of CO ₂ -Laser Radiation in CdGeAs ₂	11
D. Scalable and Efficient 9.36-μm Third-Harmonic Generation Using a Double-Pass Geometry	13
E. Investigation of Hg ₂ * as a Discharge-Pumped Optical Storage Medium	15
F. Efficient Thallium Photodissociation Laser	16
G. Real-Time Spectral Analysis of Far-Infrared-Laser Pulses Using a SAW Dispersive Delay Line	18
 III. MATERIALS RESEARCH	 23
A. Utilization of Sn-Doped In ₂ O ₃ (ITO) Films in Fabrication of GaAs Solar Cells	23
B. Temperature-Profile Calculations for a Semiconductor Heated by a Scanned CW Laser	26
 IV. MICROELECTRONICS	 31
A. Charge-Coupled Devices: SAW/CCD Buffer Memory	31
B. Binary Synthetic Holograms	32
 V. SURFACE-WAVE TECHNOLOGY	 35
A. Automated Pulsed Technique for Measuring Phase and Amplitude Response of SAW Devices	35
1. Measurement of Phase Response	35
2. Measurement of Insertion Loss	39
B. SAW Phase Shifts Due to Propagation in Shallow-Groove Gratings	41

INTRODUCTION

I. SOLID STATE DEVICE RESEARCH

Several 12-element HgCdTe 10.6- μm photodiode arrays have been fabricated and tested with average heterodyne sensitivities better than 4.8×10^{-20} W/Hz and 7.5×10^{-20} W/Hz at 760 MHz and 1.5 GHz, respectively. Typical quantum efficiencies have now been increased to the range of 70 to 85 percent. Optimum performance in the heterodyne mode of operation was obtained using 0.3 to 0.6 mW of CO_2 local-oscillator power, which produced a 2- to 4-mA photocurrent.

The residual impurity concentration in molecular-beam epitaxially grown GaAs films was found to be reduced by a factor of about 50 to approximately $4 \times 10^{15} \text{ cm}^{-3}$ when hydrogen is introduced during deposition. The band-edge photoluminescence was enhanced, whereas the deep-level photoluminescence decreased as the purity of the films increased.

II. QUANTUM ELECTRONICS

Continuous tuning of the CW Ni:MgF_2 laser has been achieved over a 460-cm^{-1} range from 1.61 to 1.74 μm . The system employed a 1.33- μm Nd:YAG pump laser and an intracavity birefringent filter.

Lasing has been observed in $\text{K}_5\text{NdLi}_2\text{F}_{10}$, a new high-Nd-concentration material. The product of lifetime and cross section is larger than that in $\text{NdP}_5\text{O}_{14}$, and the temperature and Nd concentration dependence of the lifetime are also different.

Efficient third-harmonic generation can be obtained by placing two nonlinear crystals in tandem, with the first oriented for second-harmonic generation and the second for sum mixing. By using such a two-step technique, frequency tripling of CO_2 mini-TEA laser radiation has been carried out in CdGeAs_2 with an average external conversion efficiency of 1.5 percent.

A double-pass tight-focusing geometry having a confocal parameter of only 1.0 cm was used with 8-nsec CO_2 laser input pulses to obtain 4-percent energy conversion efficiency for third-harmonic generation in a liquid $\text{CO}_2\text{-O}_2$ mixture.

Experiments to investigate the feasibility of optical energy extraction from molecular mercury with an infrared laser have been performed. An infrared-induced enhancement has been observed at 300 nm, which is 10 times the thermal value.

An efficient thallium laser at 535 and 337.6 nm has been developed based on the photolysis of thallium iodide with the 193-nm output of an ArF laser. An energy efficiency of 14 percent has been measured for conversion of the pump into the thallium laser emission.

Harmonic heterodyne detection in conjunction with a surface-acoustic-wave (SAW) dispersive delay line has been used to perform real-time spectral analysis of submillimeter laser signals. Detailed information on the longitudinal modes and spectral bandwidth of the pulsed D_2O laser ($385\text{ }\mu\text{m}$) has been obtained for the first time using this technique.

III. MATERIALS RESEARCH

A technique has been developed for using ion-beam sputtering to deposit highly transparent, highly conducting Sn-doped In_2O_3 (ITO) films for possible applications in GaAs solar cells. In initial experiments, such films have been utilized in two types of cells: those in which an ITO/p-GaAs heterojunction forms the charge-separation barrier, and shallow-homojunction cells in which the ITO forms a transparent ohmic contact to the upper n^+ -GaAs layer.

To assist in the development of experimental techniques for using laser heating to crystallize semiconductor films and to anneal ion-implantation damage in semiconductors, a theoretical model has been developed for calculating the temperature profiles of semiconductor samples heated with a scanned CW laser to temperatures below their melting points. Computer calculations utilizing this model have been carried out both for thin semiconductor films on metal-coated insulating substrates and for ion-implanted semiconductor samples.

IV. MICROELECTRONICS

The first prototype of the SAW/CCD buffer memory device has been tested at a CCD clock frequency of 100 kHz and at input signal frequencies between 80 and 130 MHz. The device operates without frequency folding between 85.6 and 128.3 MHz, within 300 kHz of the predicted values. The amplitude and phase of the output signal from the CCD track those of the input signal to the SAW device, as expected.

Two holographic masks have been fabricated which will act as lenses to convert a uniform laser-beam profile to a spherical wavefront. These masks are synthetic coding holograms, and consist of arrays of rectangular apertures built up from a minimum rectangle, which in this case was $3 \times 45\text{ }\mu\text{m}$.

V. SURFACE-WAVE TECHNOLOGY

A technique has been developed for precisely determining the phase and amplitude response of SAW devices over the relatively long delays and large bandwidths usually encountered in the devices. Measurements are made in a pulsed mode so that a number of sequential signals may be time resolved. A computer-controlled measurement system provides for the precise and rapid accumulation, analysis, and display of data from devices with time-bandwidth products of several thousand for frequencies up to 1250 MHz.

Perturbations in surface-wave propagation caused by coupling to nonpropagating bulk waves in shallow oblique- and normal-incidence groove gratings have been measured. Phase shifts upon transmission and shifts in fundamental stop-band frequency f_0 have been determined and compared with previous measurements of the magnitude of the reflection at the stop band near $2f_0$. The comparisons indicate a limitation of an existing model of grating interactions.

REPORTS ON SOLID STATE RESEARCH

15 May through 15 August 1978

PUBLISHED REPORTS

Journal Articles

<u>JA No.</u>			
4753	Surface Relief Gratings of 3200-Å-Period Fabrication Techniques and Influence on Thin-Film Growth	D. C. Flanders H. I. Smith	J. Vac. Sci. Technol. <u>15</u> , 1001 (1978)
4755	Doppler-Limited Spectra of the C-H Stretching Fundamentals of Formaldehyde	A. S. Pine	J. Mol. Spectrosc. <u>70</u> , 167 (1978)
4776	Explanation of the 6-Fold LEED Patterns from Polar (0001) and (000 $\bar{1}$) ZnO Surfaces	V. E. Henrich H. J. Zeiger E. I. Solomon* R. R. Gay*	Surf. Sci. <u>74</u> , 682 (1978)
4790	Wavelength Dependence of GaAs Directional Couplers and Electro-optic Switches	F. J. Leonberger J. P. Donnelly C. O. Bozler	Appl. Opt. <u>17</u> , 2250 (1978)
4793	1-mJ Line-Tunable Optically Pumped 16 μ m Laser	R. M. Osgood, Jr.	Appl. Phys. Lett. <u>32</u> , 564 (1978)
4799	Ultraviolet Photoemission Measurements of the Band Structure of TiO _x ($0.93 \leq x \leq 1.15$)	V. E. Henrich H. J. Zeiger T. B. Reed*	Phys. Rev. B <u>17</u> , 4121 (1978)
4803	Vibrational Energy Relaxation and Exchange in Liquid N ₂ -CO-OCS Mixtures	S. R. J. Brueck R. M. Osgood, Jr.	J. Chem. Phys. <u>68</u> , 4941 (1978)
4811	Surface Defects and the Electronic Structure of SrTiO ₃ Surfaces	V. E. Henrich G. Dresselhaus H. J. Zeiger	Phys. Rev. B <u>17</u> , 4908 (1978)
4815	Far-IR Heterodyne Radiometric Measurements With Quasioptical Schottky Diode Mixers	H. R. Fetterman P. E. Tannenwald B. J. Clifton C. D. Parker W. D. Fitzgerald N. R. Erickson*	Appl. Phys. Lett. <u>33</u> , 151 (1978)

* Author not at Lincoln Laboratory.

Meeting Speeches

MS No.

- | | | | |
|------|---|---|--|
| 4436 | Photoemission Studies of Molecular Adsorption on Oxide Surfaces | V. E. Henrich | In <u>Inelastic Electron Tunneling Spectroscopy</u> , T. F. Wolfram, Ed. (Springer-Verlag, New York, 1978), p. 160 |
| 4437 | Alignment of X-Ray Lithography Masks Using a New Interferometric Technique - Experimental Results | S. Austin
H. I. Smith
D. C. Flanders | J. Vac. Sci. Technol. <u>15</u> , 984 (1978) |
| 4438 | Polyimide Membrane X-Ray Lithography Masks - Fabrication and Distortion Measurements | D. C. Flanders
H. I. Smith | J. Vac. Sci. Technol. <u>15</u> , 995 (1978) |
| 4543 | Chemisorbed Phases of O ₂ on TiO ₂ and SrTiO ₃ | V. E. Henrich
G. Dresselhaus
H. J. Zeiger | J. Vac. Sci. Technol. <u>15</u> , 534 (1978) |
| 4544 | Surface Photovoltage Experiments on SrTiO ₃ Electrodes | J. G. Mavroides
D. F. Kolesar | J. Vac. Sci. Technol. <u>15</u> , 538 (1978) |
| 4651 | Acoustoelectric Surface Wave Devices for Programmable Signal Processing | J. H. Cafarella | <u>1978 IEEE International Symposium on Circuits and Systems Proceedings</u> (IEEE, New York, 1978), pp. 392-399 |
| 4689 | New Applications of Submicrometer Structures in Materials Science and Biology | H. I. Smith
D. C. Flanders
D. C. Shaver | Proc. Scanning Electron Microscopy '78, Los Angeles, 17-21 April 1978, Vol. I, pp. 33-40 |

* * * * *

UNPUBLISHED REPORTS

Journal Articles

JA No.

- | | | | |
|-------|--|--|---------------------------------|
| 4791A | Surface States on n-Type SrTiO ₃ | S. Ellialtioglu*
T. Wolfram*
V. E. Henrich | Accepted by Solid State Commun. |
| 4809 | High Na ⁺ -Ion Conductivity in Na ₅ YSi ₄ O ₁₂ | H. Y-P. Hong
J. A. Kafalas
M. Bayard | Accepted by Mater. Res. Bull. |
| 4814 | Optical and Electrical Properties of CdGeAs ₂ | G. W. Iseler
H. Kildal
N. Menyuk | Accepted by J. Electron. Mater. |

* Author not at Lincoln Laboratory.

JA No.

4823	Vapor Phase Growth of $\text{Hg}_{1-x}\text{Cd}_x\text{Te}$ Epitaxial Layers	P. Vohl C. M. Wolfe*	Accepted by J. Electron. Mater.
4826	Thermal Conductivity and Specific Heat of $\text{NdP}_5\text{O}_{14}$	S. R. Chinn W. K. Zwicker*	Accepted by J. Appl. Phys.
4835	Condon Internal Diffraction in the $\text{O}_u^+ \rightarrow \text{O}_g^+$ Fluorescence of Photo-associated Hg_2	D. J. Ehrlich R. M. Osgood, Jr.	Accepted by Phys. Rev. Lett.
4841	Λ -Doubling in the $v = 0 \rightarrow 2$ Overtone Band in the Infrared Spectrum of NO	A. S. Pine J. W. C. Johns* A. G. Robiette*	Accepted by J. Mol. Spectrosc.
4847	Molecular-Beam Tunable-Diode-Laser Subdoppler Spectroscopy of a Λ -Doubling in Nitric Oxide	A. S. Pine K. W. Nill*	Accepted by J. Mol. Spectrosc.
4856	Gap-Coupled InSb/LiNbO_3 Acoustoelectric Convolver Operating at 77 K	F. J. Leonberger R. W. Ralston S. A. Reible	Accepted by Appl. Phys. Lett.

Meeting Speeches†

MS No.

4540A	Efficient Infrared Third Harmonic Generation in Cryogenic Liquids	H. Kildal S. R. J. Brueck	IX Natl. Conf. on Lasers and Nonlinear Optics, Leningrad, USSR, 13-16 June 1978
4577	High Na^+ -Ion Conductivity in $\text{Na}_5\text{YSi}_4\text{O}_{12}$	H. Y-P. Hong J. A. Kafalas M. Bayard	28th Power Sources Symp., Atlantic City, New Jersey, 12-15 June 1978
4578	NASICON, A New Solid Electrolyte for Na-S Batteries	J. A. Kafalas H. Y-P. Hong	
4578A	NASICON, A New Solid Electrolyte for Na-S Batteries	J. A. Kafalas	Seminar, Environmental Impact Corp., Waltham, Massachusetts, 18 May 1978
4589	High-Efficiency GaAs Shallow-Homojunction Solar Cells	J. C. C. Fan C. O. Bozler	13th IEEE Photovoltaic Specialists Conf., Washington, DC, 5-8 June 1978
4616	Fabrication and Properties of New Solid Electrolytes	J. A. Kafalas H. Y-P. Hong	American Ceramics Society Mtg., Detroit, Michigan, 6-11 May 1978

* Author not at Lincoln Laboratory.

† Titles of Meeting Speeches are listed for information only. No copies are available for distribution.

MS No.

4620	Submicrometer Spatial Period Surface Relief Gratings for Orienting Crystalline Overlayers	D. C. Flanders D. C. Shaver H. I. Smith	8th Intl. Conf. on Electron and Ion Beam Science and Technology, Seattle, Washington, 21-26 May 1978
4625	Lasing and Fluorescence in $K_5NdLi_2F_{10}$	A. Lempicki* B. McCollum* S. R. Chinn H. Y-P. Hong	10th Intl. Quantum Electronics Conf., Atlanta, Georgia, 29 May - 1 June 1978
4639	Studies of Electronically Excited Hg_2 for Use as a Laser Storage Medium	D. J. Ehrlich R. M. Osgood, Jr.	
4643	Infrared Double Resonance of Highly Vibrationally Excited SF_6	S. R. J. Brueck T. F. Deutsch	
4644	Laser Induced Breakdown of Cryogenic Liquids	S. R. J. Brueck H. Kildal	
4650	Efficient CW Optically Pumped $Ni:MgF_2$ Laser	P. F. Moulton A. Mooradian	
4742	High Resolution Double Resonance Spectroscopy of $v_3 = 2 \leftarrow 1$ Transitions in SF_6	P. F. Moulton A. Mooradian	
4743	Efficient Third Harmonic Generation in Liquid $CO-O_2$ Mixtures	S. R. J. Brueck H. Kildal	Intl. Luminescence Conf., Paris, 17 July 1978
4625A	Luminescence of New Stoichiometric Nd^{3+} Compounds	A. Lempicki* B. McCollum* S. R. Chinn H. Y-P. Hong	
4648	$GaInAsP/InP$ Lasers and Detectors for Fiber Optic Communications at $1.1 - 1.3 \mu m$	J. J. Hsieh C. E. Hurwitz C. C. Shen	Electro '78 - Optical Guided Wave Transmission Technology, Boston, 23-25 May 1978
4656	Submillimeter Wavelength Surface Oriented Diode Mixers	R. A. Murphy G. D. Alley C. O. Bozler H. R. Fetterman P. E. Tannenwald B. J. Clifton	1978 IEEE-MTT-S Symp., Ottawa, Ontario, Canada, 27-29 June 1978
4658	High Sensitivity Submillimeter Heterodyne Receiver	H. R. Fetterman P. E. Tannenwald B. J. Clifton C. D. Parker W. D. Fitzgerald N. R. Erickson*	

* Author not at Lincoln Laboratory.

MS No.			
4701	Solid State Electrochromic Displays Using Solid Electrolytes	M. Bayard	Electronic Materials Conf., Santa Barbara, California, 28-30 June 1978
4702	Effect of H ₂ on Residual Impurities in GaAs MBE Layers	A. R. Calawa	
4708	Synthesis and Crystal Growth of CdGeP ₂	P. Vohl	
4703	Self-Broadening and ¹³ C/ ¹² C Isotope Intensity Ratios in the ν_3 -Band of Methane	A. S. Pine	Molecular Spectroscopy Symp., Ohio State University, Columbus, 12-16 June 1978
4704	Torsional Splittings and Assignments in the Low Temperature Doppler-Limited Spectrum of the C-H Stretching Bands of Ethane	A. S. Pine W. J. Lafferty*	
4705	Λ -Doubling in the $\nu = 0 \rightarrow 2$ Overtone of NO	A. S. Pine J. W. C. Johns* A. G. Robiette*	
4730	The Growth of Large, Laser Quality Nd _x La _{1-x} P ₅ O ₁₄ Crystals	W. K. Zwicker* T. Kovats* S. R. Chinn	4th American Conf. on Crystal Growth, National Bureau of Standards, Gaithersburg, Maryland, 16-20 July 1978
4731	UPS Studies of the Chemisorption of CO, NH ₃ and H ₂ O on ZnO	R. R. Gay E. I. Solomon* V. E. Henrich H. J. Zeiger	38th Physical Electronics Conf., Oak Ridge National Laboratory, Oak Ridge, Tennessee, 19-21 June 1978

* Author not at Lincoln Laboratory.

ORGANIZATION

SOLID STATE DIVISION

A. L. McWhorter, *Head*
I. Melngailis, *Associate Head*
C. R. Grant, *Assistant*

R. H. Kingston, *Senior Staff*
P. E. Tannenwald, *Senior Staff*

QUANTUM ELECTRONICS

A. Mooradian, *Leader*
P. L. Kelley, *Associate Leader*

Barch, W. E.	Fleming, M. W.*
Belanger, L. J.	Hancock, R. C.
Blumberg, W. A. M.	Kildal, H.
Brueck, S. R. J.	Menyuk, N.
Burke, J. W.	Moulton, P. F.
Chinn, S. R.	Osgood, R. M., Jr.
DeFeo, W. E.	Parker, C. D.
Deutsch, T. F.	Peck, D. D.
Ehrlich, D. J.	Pine, A. S.
Fetterman, H. R.	

APPLIED PHYSICS

A. G. Foyt, *Leader*
C. E. Hurwitz, *Assistant Leader*
T. C. Haman, *Senior Staff*

Armiento, C. A.*	Leonberger, F. J.
Calawa, A. R.	Lind, T. A.
Carter, F. B.	Maby, E.*
DeMeo, N. L., Jr.	McBride, W. F.
Diadiuk, V.*	Paladino, A. E.
Donnelly, J. P.	Plonko, M. C.
Duffy, P. E.	Spears, D. L.
Ferrante, G. A.	Tsang, D. Z.*
Glasser, L. A.*	Walpole, J. N.
Groves, S. H.	

ELECTRONIC MATERIALS

A. J. Strauss, *Leader*
H. J. Zeiger, *Associate Leader*
J. G. Mavroides, *Senior Staff*

Anderson, C. H., Jr.	Hong, H. Y-P.
Bayard, M. L.	Hsieh, J. J.
Button, M. J.	Iseler, G. W.
Cava, R. J.*	Kafalas, J. A.
Chapman, R. L.	Kolesar, D. F.
Davis, F. M.	Krohn, L., Jr.
Delaney, E. J.	Mastromattei, E. L.
Fahey, R. E.	Owens, E. B.
Fan, J. C. C.	Palm, B. J.
Feldman, B.	Pantano, J. V.
Finn, M. C.	Smith, D. D.
Gale, R. P.	Tracy, D. M.
Gay, R. R.*	Vohl, P.
Henrich, V. E.	

SURFACE WAVE TECHNOLOGY

E. Stern, *Leader*
R. C. Williamson, *Associate Leader*

Baker, R. P.	LaFleur, W. J.
Brogan, W. T.	Melngailis, J.
Cafarella, J. H.	Oates, D. E.
Dolat, V. S.	Ralston, R. W.
Holtham, J. H.	Reible, S. A.
Hurlburt, D. H.	Slattery, R. L.
Kernan, W. C.	

MICROELECTRONICS

W. T. Lindley, *Leader*
F. J. Bachner, *Associate Leader*
H. I. Smith, *Assistant Leader*

Alley, G. D.	Grant, L. L.
Beatrice, P. A.	Gray, R. V.
Bozler, C. O.	Hansell, G. L.*
Burke, B. E.	Hawryluk, A. M.*
Chiang, A. M.	Lincoln, G. A., Jr.
Clifton, B. J.	McGonagle, W. H.
Clough, T. F.	Mountain, R. W.
Daniels, P. J.	Murphy, R. A.
DeGraff, P. D.	Pichler, H. H.
Durant, G. L.	Shaver, D. C.*
Efremow, N., Jr.	SilverSmith, D. J.
Elta, M. E.	Smythe, D. L., Jr.
Felton, B. J.	Turner, G.
Flanders, D. C.	Wilde, R. E.
Geis, M. W.	

* Research assistant

L. SOLID STATE DEVICE RESEARCH

A. 12-ELEMENT HgCdTe PHOTODIODE ARRAYS

Several 12-element HgCdTe 10.6- μm photodiode arrays with average heterodyne sensitivities better than 4.8×10^{-20} W/Hz at 760 MHz and 7.5×10^{-20} W/Hz at 1.5 GHz have been fabricated and tested. This improved performance over that previously reported for the 12-element arrays¹ was due primarily to the implementation of a highly effective ZnS antireflection coating. A typical 1.1- μm -thick ZnS film was found to increase the quantum efficiency at 10.6 μm by a factor of 1.4, which was very close to the value of 1.45 expected for an ideal AR coating. Thus, the typical 50- to 60-percent quantum efficiencies¹ have now been increased to 70 to 85 percent without any degradation in diode characteristics.

Optimum performance in the heterodyne mode of operation was obtained with these devices using 0.3 to 0.6 mW of CO₂ local-oscillator (LO) power, which produced 2- to 4-mA photocurrents. Near this optimum LO power the sensitivity was not a strong function of LO power, a 50-percent variation having little effect. However, a large drop in heterodyne sensitivity is produced by greatly increasing or decreasing the LO power. Table I-1 lists some heterodyne performance parameters at 760 MHz for two typical HgCdTe photodiodes under optimum operating conditions. Blackbody heterodyne measurements were made to determine an effective heterodyne quantum efficiency² and the corresponding equivalent receiver noise figure. An attempt to account for our observed sensitivity values by taking into consideration the primary factors affecting wide-bandwidth heterodyne sensitivity is made in Table I-1. At the optimum operating LO power, the amplifier noise contribution (28 and 36 percent of the total noise) was small but significant. The frequency-dependent part of the junction collection efficiency, which is due to slow carrier diffusion to the junction, was estimated from pulse-response data;² a 15-percent

TABLE I-1 HETERODYNE PERFORMANCE FACTORS AT 760 MHz (for Two Typical HgCdTe Photodiodes)		
	61B-T4-1	60A-T3-2
Effective Heterodyne Quantum Efficiency (percent)	48.0	40.0
Equivalent Receiver Noise Figure (dB)	3.2	4.0
Degradation Factors		
Amplifier noise (NF = 2.6 dB)	1.4 dB (28%)	1.9 dB (36%)
Photodiode quantum efficiency (low power)	0.9 dB (82%)	1.1 dB (78%)
Junction collection efficiency (~85 percent at 760 MHz)	0.7 dB	0.7 dB
	3.0 dB	3.7 dB

TABLE I-2 HETERODYNE SENSITIVITY AND UNIFORMITY AT 10.6 μm OF SIX 12-ELEMENT HgCdTe PHOTODIODE ARRAYS			
Array	Average Sensitivity (W/Hz)		Sensitivity Variation Within Array (percent)
	At 760 MHz	At 1500 MHz	
61B-T4	4.3×10^{-20}	7.1×10^{-20}	± 13
60A-T4	4.6	—	12
60A-T3	4.7	7.5	5
61B-T5	4.7	7.4	10
60A-T2	Δ 6.0 (4.5)	—	12
61B-T1	Δ 6.0 (4.5)	—	8
Δ measurements made before AR coating.			

TABLE I-3 ELECTRICAL CHARACTERISTICS OF GaAs MBE FILMS GROWN WITH AND WITHOUT HYDROGEN						
Dopant	Hydrogen Pressure (Torr)	Carrier Type	Carrier Concentration (10^{15} cm^{-3})		Carrier Mobility ($\text{cm}^2/\text{V sec}$)	
			300 K	77 K	300 K	77 K
Undoped	—	p	4.0	0.5	220	270
	1×10^{-6}	p	3.0	0.3	390	4,900
Si (750°C)	—	p	3.6	1.7	290	1,800
	1×10^{-6}	n	2.0	2.0	7,200	28,100
Si (900°C)	—	n	10.0	8.5	2,800	3,500
	2×10^{-6}	n	12.0	9.7	6,300	18,500

slow-decay component was observed in the response characteristics of these diodes. The close agreement between our calculated sensitivity degradation factors and the equivalent receiver noise figure indicates that, at the optimum operating point, high-power saturation effects are not significant. The existence of the frequency-dependent part of the collection efficiency factor is particularly detrimental to device performance, as it not only decreases the signal level but effectively adds to the noise, since the slowly diffusing carriers also contribute shot noise.

Both the quantum efficiency and the junction collection efficiency decrease with increasing LO power. These reduced efficiencies are a consequence of the high excess photoelectron concentrations resulting in conduction-band filling and reduced optical absorption and carrier lifetimes. All three degradation factors listed in Table I-1 are LO-power dependent. Increasing the LO power will decrease the amplifier noise effect but at a cost in reduced quantum efficiency and junction collection efficiency, such that there is a net loss in heterodyne sensitivity.

About ten 12-element HgCdTe photodiode arrays have been tested for heterodyne sensitivity at 760 and 1500 MHz using blackbody radiometry. One element of the array was used to establish an optimum bias voltage and LO-power level, and then the sensitivities of the other 11 elements were measured using the same bias and power level. Typical values were 0.5 V and 0.4 mW. The results of these measurements on six arrays are summarized in Table I-2 where the average heterodyne sensitivity and uniformity at 760 MHz are given. Three of these devices were also evaluated at 1500 MHz. The bottom two arrays were tested before the AR coatings were applied; the numbers in parentheses are estimated values with the AR coating. Four arrays have yielded average sensitivities better than 4.8×10^{-20} W/Hz at 760 MHz and 7.5×10^{-20} W/Hz at 1500 MHz. All six arrays have shown very good sensitivity uniformity, ranging from $\pm 5\%$ to $\pm 13\%$ extreme variation from element-to-element within each array.

D. L. Spears

B. EFFECT OF H₂ ON RESIDUAL IMPURITIES IN GaAs MBE LAYERS

The residual impurity concentration in molecular-beam epitaxially grown GaAs films is significantly reduced when hydrogen is introduced during deposition. The electrical characteristics of some GaAs MBE films grown with and without hydrogen are shown in Table I-3. These data were obtained from films grown at 1 $\mu\text{m/hr}$ at a substrate temperature of 575°C and an As₄/Ga atom concentration ratio of 5. For these experiments, two semi-insulating GaAs substrates were mounted in the system on separate substrate holders. Then, 3- μm -thick single layers were grown consecutively on the two substrates – first without hydrogen, then with the designated hydrogen in the system. All other growth parameters were kept constant. The results of three runs are shown in Table I-3 for different doping levels. Both unintentionally doped films are p-type. With 10^{-6} Torr of hydrogen, however, the carrier concentration is reduced by about a factor of 2 and the mobility is significantly increased. With the silicon-source temperature at 750°C, the layer without hydrogen remained p-type, while the one grown with hydrogen was n-type. At a silicon source temperature of 900°C, both layers were n-type. As indicated by the large difference in 77 K mobilities, the films grown without hydrogen were highly compensated and had total ionized impurity concentrations $>10^{17} \text{ cm}^{-3}$. The effect of hydrogen on residual impurity compensation is graphically illustrated in Fig. I-1. The net donor concentrations $N_D - N_A$ were obtained from Hall measurements, whereas the total ionized impurity concentrations $N_D + N_A$ were obtained from 77 K mobility analysis.³ It is clear that substantial

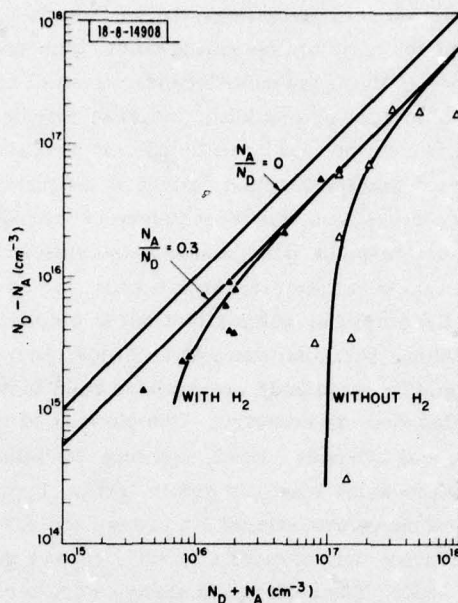


Fig. I-1. Net donor concentration $N_D - N_A$ as a function of total ionized impurity concentration $N_D + N_A$ with and without hydrogen. Lines for uncompensated GaAs, $N_A/N_D = 0$, and 30-percent compensation, $N_A/N_D = 0.3$, are drawn for reference.

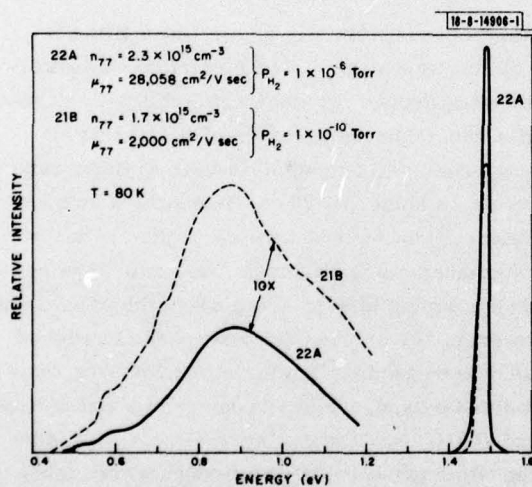


Fig. I-2. Effect of H_2 ambient pressure on band-edge (1.49 eV) and deep-level photoluminescence in n-GaAs MBE films.

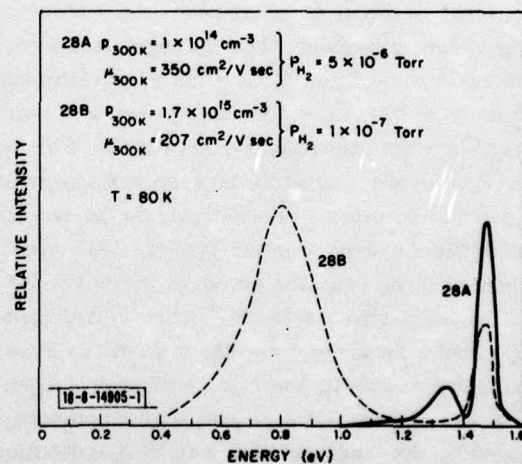
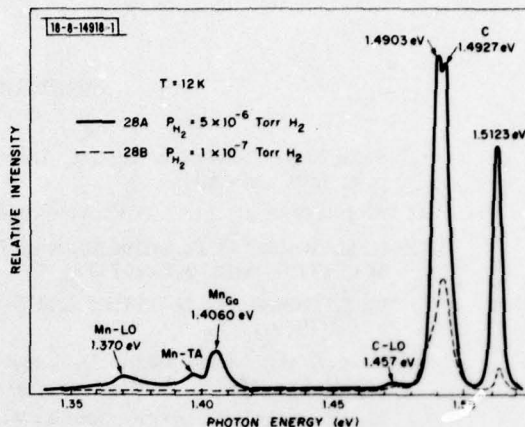


Fig. I-3. Effect of H_2 ambient pressure on band-edge (1.49 eV) and deep-level photoluminescence in p-GaAs MBE films.

reductions in $N_D + N_A$ have been achieved. As shown in Fig. I-1, a reduction of 50 times was attained for films with the lowest net donor concentrations.

Results of photoluminescence measurements made at 80 K on two n-type silicon-doped films and on two p-type undoped films with different hydrogen pressures are shown in Figs. I-2 and I-3, respectively. The electrical characteristics of each film are shown in the insets. The dominant effects of the hydrogen in each case are the large reduction in intensity of deep-level luminescence and an increase in band-edge luminescence. The deep-level luminescence with maxima at 0.88 eV in the n-type films and at 0.80 eV in the p-type samples is believed to be due to oxygen or oxygen complexes.⁴

Fig. I-4. Effect of H_2 ambient pressure on band-edge photoluminescence in p-GaAs MBE films.



The band-edge luminescence spectra for samples 28A and 28B were examined more closely at 10 K and are shown in Fig. I-4. The peak at 1.512 eV is attributed to recombination of an exciton bound to a neutral acceptor, and the double peaks at 1.4927 and 1.4903 eV are believed to be due to free electron to carbon acceptor and donor to carbon acceptor pair transitions, respectively.⁵ Although this doublet is not always seen, the relative intensity of the 1.512-eV peak always increases relative to the carbon acceptor transitions when excess hydrogen is added during growth. This result suggests that the number of carbon acceptors is reduced when H_2 is present. The peak at 1.4060 eV is attributed to Mn on a Ga site.⁶ Phonon replicas are also observed.

It appears that the dominant effect of the introduction of hydrogen during MBE growth is to reduce the incorporation of oxygen in the epitaxial layer. It may also be inferred from the 10 K photoluminescence results and from the reduction in acceptor concentration that less carbon is introduced into the GaAs epilayer when the hydrogen is present. Carbon and oxygen are the major constituents of the residual gases in the vacuum system, which are predominantly CO_2 , CO , O_2 , H_2O , and several hydrocarbons. Although the partial pressures of these gases are in the range of 10^{-10} to 10^{-11} Torr, they are in quantity adequate to dope the films at the observed levels even with sticking coefficients as low as 10^{-3} .

It is clear that the lower limit of the total impurity concentration will depend on source and system contaminants as well as residual gas levels. As indicated in Fig. I-1, this limit may not have been reached in these experiments, and further reduction should be possible by careful adjustment of incident dopant flux and of surface stoichiometry.

A. R. Calawa
J. G. Mavroides

REFERENCES

1. Solid State Research Report, Lincoln Laboratory, M.I.T. (1978:1), p. 1, DDC AD-A056715.
2. Ibid. (1976:3), p. 5, DDC AD-A034647/8.
3. C. M. Wolfe, G. E. Stillman, and J. O. Dimmock, J. Appl. Phys. 41, 504 (1970), DDC AD-707572.
4. W. J. Turner, G. D. Pettit, and N. G. Ainslie, J. Appl. Phys. 34, 3274 (1963).
5. A. M. White, P. J. Dean, D. J. Ashen, J. B. Mullin, M. Webb, B. Day, and P. D. Greene, J. Phys. C: Solid State Phys. 6, L243 (1973).
6. M. Illegems, R. Dingle, and L. W. Rupp, Jr., J. Appl. Phys. 7, 3059 (1975).

II. QUANTUM ELECTRONICS

A. TUNABLE Ni:MgF₂ LASER

A CW-pumped Ni:MgF₂ laser has been operated in a 3-mirror cavity with a birefringent tuning element, and has been continuously tuned over a 460-cm^{-1} range from 1.61 to $1.74\text{ }\mu\text{m}$.

A schematic diagram of the 3-mirror cavity is shown in Fig. II-1. Two of the mirrors are inside the vacuum section of a liquid nitrogen Dewar. The angle between the two arms of the cavity is chosen such that the astigmatism introduced by a 1-cm -long Ni:MgF₂ Brewster-angle crystal is canceled by that of the spherical mirror.¹ The design yields a minimum beam area of about $1.5 \times 10^{-4}\text{ cm}^2$ for the TEM₀₀ mode inside the crystal. The tuning element is a single plate of crystalline quartz, 1.4 mm thick, oriented with the "c"-axis 57° away from the surface normal.

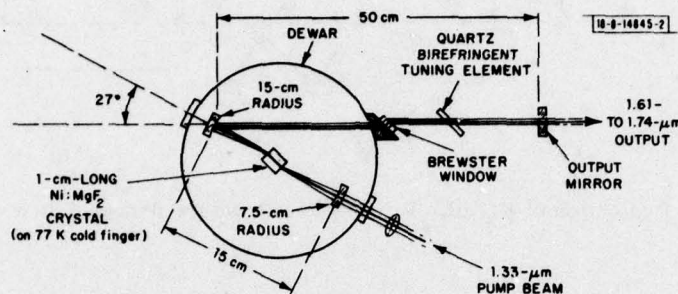


Fig. II-1. Diagram of Ni:MgF₂ 3-mirror-cavity laser.

Initial results have been obtained with a $0.65\text{-wt}\%$ Ni crystal, which absorbs about 50 percent of the $1.33\text{-}\mu\text{m}$ pump radiation. The lowest absorbed power laser threshold was 22 mW , found with a 0.2-percent transmission output mirror and no tuning element in the cavity. The TEM₀₀ pump beam radius at the crystal was about $50\text{ }\mu\text{m}$. In Fig. II-2 we show the power-output-vs-wavelength curve for the laser with the tuning element inserted, with a 1-percent transmission

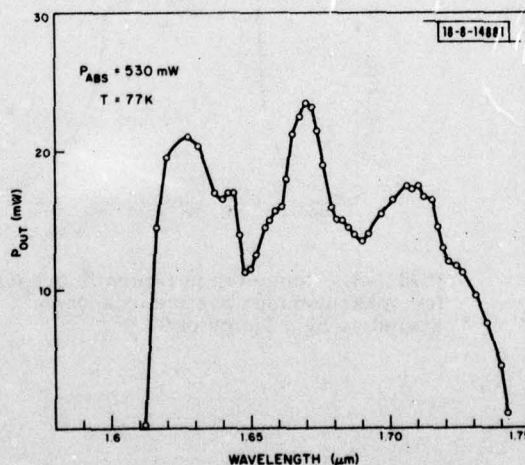


Fig. II-2. Power output vs wavelength for Ni:MgF₂ laser.

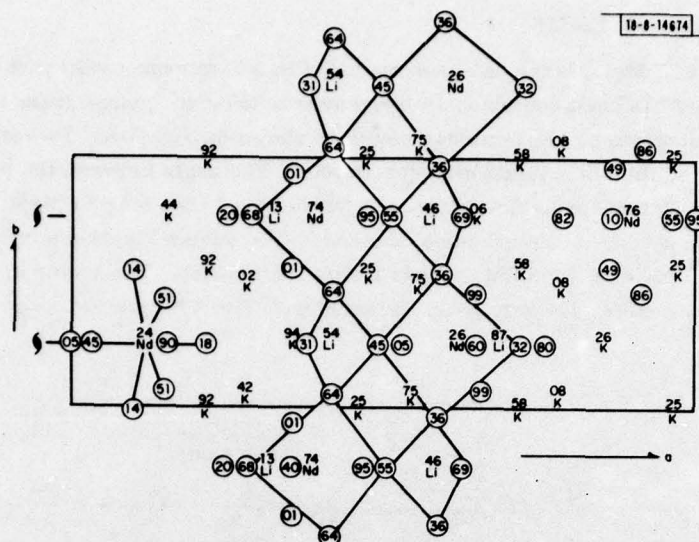


Fig. II-3. Projection of $K_5NdLi_2F_{10}$ crystal structure perpendicular to c-axis.

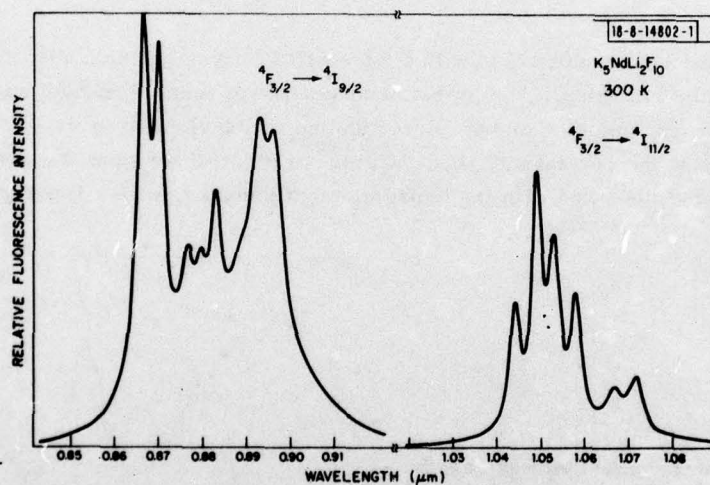


Fig. II-4. Room-temperature fluorescence of $K_5NdLi_2F_{10}$, uncorrected for measurement system response. The 1.05- μm spectrum should be scaled up by a factor of 9.

output mirror, and for an absorbed pump power of 530 mW. The maxima in output power correspond to maxima in the fluorescence spectrum. The lowest laser threshold for this configuration was about 90 mW.

For the ratio of pump power to threshold pump power achieved in the measurements indicated in Fig. II-2, we expect a wider tuning range and more output power than observed. The total cavity loss as a function of pump power was determined by ringing frequency measurements² and was found to be constant, about 2.8 percent, with a 1-percent output coupler but no tuning element. Thus, pump-power dependent losses, which would affect the actual pumping ratio, were not being generated in the crystal. Numerical computations of the laser rate equations, taking into account the three-dimensional variation of pump intensity and laser-mode intensity inside the crystal, are being undertaken to predict the laser efficiency, both to discover how much the predictions disagree with experiment and to find the optimum size and location of the pump beam waist in the crystal.

P. F. Moulton
A. Mooradian

B. LASING AND FLUORESCENCE IN $K_5NdLi_2F_{10}$

We have synthesized a new Nd compound, $K_5NdLi_2F_{10}$ (KNLF), and have measured some of the lasing and fluorescence properties of Nd^{3+} in this material. This is the first stoichiometric Nd fluoride in which stimulated emission has been obtained, and a comparison of its characteristics with those of the recently investigated stoichiometric Nd oxides (such as NdP_5O_{14}) may provide information on some of the important energy transfer and relaxation mechanisms in these high-Nd-concentration materials.

Initially, crystals were grown from a charge of $NdF_3:9 LiF:6 KF$ in a closed graphite crucible in an argon atmosphere. After equilibration at 900°C for several hours, the charge was slowly cooled to room temperature, and small crystal platelets were manually separated from the flux matrix.

The structure and thus the composition of the crystals were determined by using the single-crystal x-ray heavy-atom method. (Now that the composition of the new material has been found, it is likely that improved crystal growth can be achieved by using a growth charge of this same composition.) The space group is orthorhombic, $Pnma$, with lattice constants $a = 20.6519 \text{ \AA}$, $b = 7.7787 \text{ \AA}$, and $c = 6.9017 \text{ \AA}$. A projection of the crystal structure is shown in Fig. II-3. The Nd point symmetry is m , with 8-fold coordination to surrounding F^- ions. The Nd^{3+} concentration is $3.61 \times 10^{21} \text{ cm}^{-3}$, and the smallest Nd-Nd separation is 6.73 \AA .

Fluorescence and lasing data were taken with a platelet $0.3 \times 0.8 \times 0.1 \text{ mm}$, with the a -axis (the lasing direction) perpendicular to the broad face. The $^4F_{3/2} \rightarrow ^4I_{9/2}$, $^4I_{11/2}$ fluorescence spectra were obtained at 300, 70, and 2 K, using CW excitation from a rhodamine-6G dye laser to pump the 580-nm Nd^{3+} absorption band. Figure II-4 shows the room-temperature fluorescence into the $^4I_{9/2}$ and $^4I_{11/2}$ manifolds. At room temperature the $^4F_{3/2} \rightarrow ^4I_{11/2}$ emission consists of six well-resolved broad peaks, with the two strongest at 1048 and 1052 nm, having full-widths $\sim 25 \text{ cm}^{-1}$. At low temperatures, the emission lines become quite narrow, indicating that the room-temperature broadening is homogeneous. Although the low Nd site symmetry m does not impose any selection rules, changes in relative intensity among the components are observed in different polarizations. The low-temperature $^4F_{3/2}$ splitting is 50 cm^{-1} , decreasing slightly to 45 cm^{-1} at room temperature. The energy levels as calculated from the

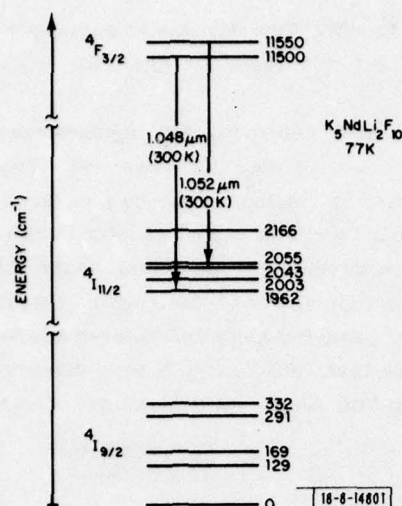


Fig. II-5. Partial energy-level diagram of $\text{K}_5\text{NdLi}_2\text{F}_{10}$, determined from 77 K fluorescence.

77 K fluorescence spectra are shown in Fig. II-5, with the dominant laser transitions at room temperature. The fluorescent lifetime of the $^4\text{F}_{3/2}$ manifold was measured using pulsed excitation in the 800-nm Nd^{3+} absorption band. The lifetime increased smoothly from 300 μsec at room temperature to 640 μsec at 2 K. This is in striking contrast to the behavior of $\text{NdP}_5\text{O}_{14}$ (NPP), in which lifetime is independent of temperature. One factor contributing to the long lifetime may be the large separation between nearest-neighbor Nd^{3+} ions.

Lifetime measurements were also made on polycrystalline samples containing the rare earth (RE) Ce or La as well as Nd, which were prepared by a different technique. X-ray-diffraction analysis showed that these samples contained some amounts of a $\text{KNd}_x(\text{RE})_{1-x}\text{F}_4$ phase, but data obtained using spectral discrimination of the emission wavelength indicated that the lifetime of the $\text{K}_5\text{Nd}_y(\text{RE})_{1-y}\text{Li}_2\text{F}_{10}$ phase changed little with Nd concentration over a considerable range of y (qualitatively estimated from the starting charge composition). Both the temperature dependence and the preliminary concentration quenching behavior indicate that the energy migration and cross-relaxation processes may be significantly different in KNLF than in the stoichiometric Nd oxides.

Laser emission was obtained with the platelet sample in the center of a nearly concentric 10-cm-long resonator. Collinear pumping by a chopped CW dye laser ($\lambda = 586 \text{ nm}$) was used, with approximately 40 percent of the pump radiation absorbed in the 98- μm -thick sample. The lowest threshold absorbed power was 1.4 mW, with a 0.2-percent transmitting output mirror. With an output transmission of 1 percent, the threshold power increased to 2.1 mW, and a 19-percent slope power efficiency was measured. Using a value for the internal round-trip loss of ~ 2 percent (calculated from the slope efficiency), we can compare the performance of KNLF with NPP under the same experimental conditions. Taking typical NPP laser parameters measured previously, we estimate that the product of the KNLF effective cross section and lifetime, $\sigma\tau$, is roughly 1.2 times that of NPP. The effective ($^4\text{F}_{3/2}$ population-weighted) cross section for KNLF at a wavelength of 1048 nm is about $0.8 \times 10^{-19} \text{ cm}^2$. At higher pump levels, emission at 1052 nm was observed, polarized orthogonally to the 1048-nm emission. Lasing was also observed with the sample mounted at Brewster's angle, but with higher threshold.

With its relatively long spontaneous fluorescent lifetime, KNLF may be an attractive candidate for miniature pulsed-laser devices in which Q-switched operation is enhanced by efficient energy storage in the laser material.

S. R. Chinn A. Lempicki†
H. Y-P. Hong B. McCollum†
M. Bayard

C. EFFICIENT, TWO-STEP FREQUENCY TRIPLING OF CO₂-LASER RADIATION IN CdGeAs₂

Second-harmonic generation (SHG) of CO₂-laser radiation has been obtained in CdGeAs₂ crystals at efficiencies in excess of 25 percent;³ however, the highest conversion efficiency reported for third-harmonic generation (THG) in CdGeAs₂ is 10⁻⁶ (see Ref. 4). Although part of the problem of obtaining high THG efficiency lies in the difficulty of obtaining crystals with acceptable optical transmission in the 3.2- to 3.6-μm range, a few such crystals have been obtained. A more fundamental limitation is due to the relative values of the third- and second-order susceptibilities in CdGeAs₂. This is shown in Eq. (II-1) which gives the relative intensities of SHG [I(2ω)] and THG [I(3ω)] for a weakly focused pump intensity I(ω) (see Ref. 5):

$$\frac{I(3\omega)}{I(2\omega)} \cong \frac{18\pi}{c} \left(\frac{c_{\Pi}}{d_{\text{eff}}} \right)^2 I(\omega) \quad (\text{II-1})$$

where c_{Π} and d_{eff} are effective third- and second-order susceptibilities, respectively. Since $(c_{\Pi}/d_{\text{eff}}) = (1.6 \pm 0.8) \times 10^{-4}$ (Ref. 5), it is clear that extremely high intensities, probably exceeding damage thresholds, would be required to achieve efficient THG. Equation (II-1) ignores absorption effects, which generally will further reduce the relative THG output.

Alternatively, frequency tripling can be achieved by a two-step process in which one crystal is used to generate a second harmonic that is then sum-mixed in a second crystal to produce the third harmonic.^{6,7} Sum-mixing efficiency is comparable to that of SHG. Hence, significant overall frequency-tripling efficiencies can be obtained using CO₂ lasers operating at easily attainable intensity levels subject, of course, to having crystals which are phase matchable and have sufficiently low absorption losses at all three frequencies.

We have carried out frequency-tripling experiments by the two-step process using a mini-TEA laser⁸ as the fundamental source and two CdGeAs₂ crystals. The first crystal was cut for type I SHG phase matching. Since CdGeAs₂ is a positive birefringent material ($n_e > n_o$), the fundamental is applied as an extraordinary wave and the second harmonic emerging from the crystal is an ordinary wave. Thus, the transmitted fundamental and the second-harmonic waves leave the crystal with mutually orthogonal polarizations.

This is the desired geometry for pumping a second CdGeAs₂ crystal cut for type II phase-matching and oriented so that, relative to the second crystal, the entering fundamental and second harmonic are ordinary and extraordinary waves, respectively. The emerging third harmonic is an ordinary wave.

The SHG crystal is 12 mm long and has yielded internal SHG conversion efficiencies up to 26 percent when pumped by the mini-TEA laser under the same conditions as those used in the frequency-tripling experiment. The mixing crystal is 4.5 mm long. The initial experiment was performed with the two crystals placed next to each other in a single liquid nitrogen Dewar.

†GTE Laboratories Incorporated, Waltham, Massachusetts.

This arrangement has the disadvantage of not permitting rotation of the crystals relative to each other to optimize each stage independently. However, a two-Dewar arrangement requires two extra windows and a refocusing lens. These elements can lead to considerable reflection and absorption losses, as well as losses due to achromatism in the lens. In addition, the greater distance involved will lead to increased walk-off loss.

The first crystal had been antireflection (AR) coated for SHG, with a transmission factor of 0.97 at $10.6\text{ }\mu\text{m}$ at the entering surface and factors of 0.96 and 0.81 at the output face for 5.3 and $10.6\text{ }\mu\text{m}$, respectively. The mixing crystal was also AR coated, with transmission factors of 0.93 and 0.84 at the input face for 5.3 and $10.6\text{ }\mu\text{m}$, respectively, and 0.96 for $3.5\text{ }\mu\text{m}$ at the output face. The mini-TEA-laser output was apertured to give a TEM_{00} mode at $10.6\text{ }\mu\text{m}$ which was weakly focused at the sample position. The calculated spot size at the sample is $w_0 \approx 700\text{ }\mu\text{m}$, and the confocal parameter $b \approx 30\text{ cm}$. The laser repetition rate was 40 Hz .

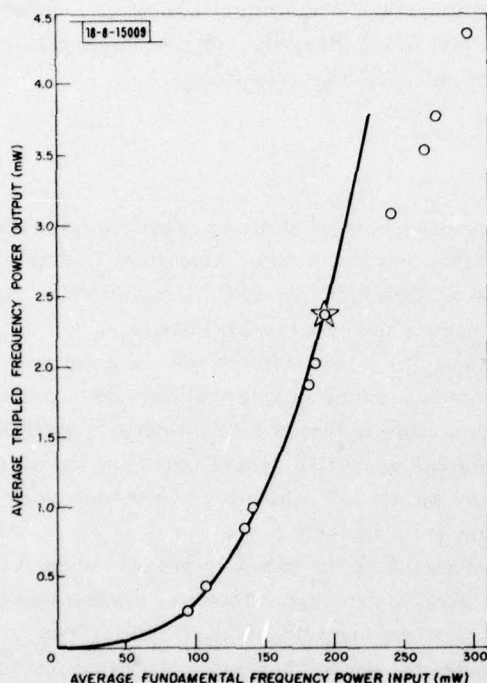


Fig. II-6. Third-harmonic output in CdGeAs_2 as a function of fundamental input power. Line is a cubic curve defined by origin and starred point.

The results of the frequency-tripling experiment are shown in Fig. II-6. Both the input and output values shown in the figure represent average power external to the Dewar. At the lower input values the third harmonic follows the expected cubic relationship, with saturation effects appearing at the higher input levels. The efficiency is still increasing at the highest point shown, which corresponds to an average external conversion efficiency of 1.5 percent. When reflection losses at the Dewar windows and crystal surfaces are taken into account, this corresponds to an overall internal conversion factor near 3 percent. In addition, the widths of the fundamental, second-, and third-harmonic pulses were approximately 90, 65, and 45 nsec, FWHM respectively, so peak conversion efficiency is about twice the average value.

The frequency-tripling conversion efficiency obtained by the two-step process is several orders of magnitude greater than that which has been obtained by THG in a single CdGeAs_2

crystal.⁴ However, efficient THG of a CO₂ laser has recently been achieved by resonant enhancement of the nonlinear susceptibility in cryogenic liquids (see Refs. 9 through 11, and Sec. D below). By this technique, conversion efficiency as high as 2 percent has been obtained with a 120-nsec CO₂-laser pulse,¹¹ and 4 percent with an 8-nsec pulse (see Sec. D below). It is estimated that 10-percent efficiency should be attainable by this method.⁹

It is of interest to consider briefly some of the relative merits of the two techniques. In addition to the simplicity of the experimental arrangement, a major advantage of frequency tripling with CdGeAs₂ crystals is that it can be obtained with all the CO₂-laser lines while the use of cryogenic liquids limits the frequencies obtainable to those for which resonant susceptibility enhancement occurs. The number of frequencies obtainable can be increased significantly by 4-wave sum- and difference-frequency mixing using two CO₂ TEA lasers, but at the cost of some added experimental complexity. On the other hand, efficient conversion by the two-step frequency-tripling process requires that the SHG crystal operate near its damage threshold, which is over an order of magnitude lower than that of the cryogenic liquid.^{9,12} A major problem is the paucity of CdGeAs₂ crystals with sufficiently low optical absorption in the 3.2- to 3.6- μ m region to be useful, and those available generally have a small cross-sectional area (4 \times 4 mm is typical).

The size limitation, coupled with the lower damage threshold, restricts the total energy which can be frequency tripled with CdGeAs₂ crystals. Hence, this technique lacks the scalability available with cryogenic liquids, which can be expanded for use at very high energies. However, its relative experimental simplicity, coupled with its ability to function at all CO₂-laser frequencies, makes frequency tripling with CdGeAs₂ crystals an attractive alternative for relatively low-energy (\lesssim 0.1 J) applications.

N. Menyuk
G. W. Iseler

D. SCALABLE AND EFFICIENT 9.36- μ m THIRD-HARMONIC GENERATION USING A DOUBLE-PASS GEOMETRY

We have extended our measurements¹³ of third-harmonic generation (THG) of the CO₂ laser in liquid CO-O₂ mixtures both by employing a double-pass configuration and by making initial measurements with a short-pulse CO₂ oscillator-amplifier system.

For nonlinear optical systems which are input energy limited, multi-pass techniques provide a straightforward enhancement of the conversion efficiency. For systems which are limited by the other effects, multi-pass techniques provide similar advantages to increases in the interaction length, but without the reduced phasematching tolerances that are inherent in longer interaction lengths. For Kerr-effect nonlinearities, multi-pass techniques allow the possibility of correcting the phase shifts and distortions of the optical waves in between passes of the nonlinear medium. This physical separation of the active nonlinear medium and the Kerr-effect compensation medium significantly enhances the experimental possibilities.

The wavevector mismatch $\Delta k = k_4 \pm k_1 \pm k_2 \pm k_3$ between the various optical waves in a 4-wave mixing experiment is an important parameter which must be controlled to optimize the process. In multi-component systems, it is often difficult to determine the relative contributions to Δk without an extensive series of measurements since variations in the relative concentrations may vary other parameters such as the nonlinear susceptibility $\chi^{(3)}$ as well as Δk . Interference effects that arise between the waves generated in each pass of a multi-pass system provide a simple method for determining Δk independent of these other effects. We have used a

double-pass system to measure $\Delta k = k_{3\omega} - 3k_{\omega}$ for THG of the CO_2 laser at 1069 cm^{-1} in liquid CO-O_2 mixtures. It is important to note that the scale of these interference fringes is set by Δk , not by k , and they therefore correspond to relatively coarse and easily measured and maintained fringe spacings. The Δk that we obtain varies linearly with CO concentration from $\Delta k_{\text{O}_2} = 3.7 \text{ cm}^{-1}$ in pure O_2 ($T = 77 \text{ K}$) to $\Delta k_{\text{CO}} = -86 \text{ cm}^{-1}$ in undiluted liquid CO at 77 K .

In the double-pass geometry, we use a mirror to refocus both the fundamental and third-harmonic beams emerging from the first pass of the liquid cell back into a nonoverlapping spatial region in the same liquid mixture (Fig. II-7). This is the first use of a multiple-pass configuration in a tight-focusing geometry where the nonlinear medium necessarily exhibits substantial wavevector mismatch between the fundamental and third-harmonic frequencies. Double-pass experiments have previously been reported¹⁴ in collimated-beam experiments ($\Delta k = 0$).

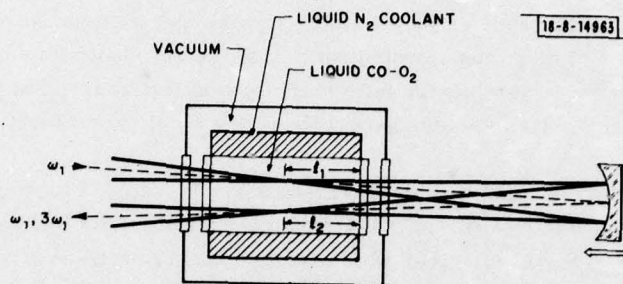


Fig. II-7. Double-pass tight-focusing geometry for THG in liquid CO-O_2 mixtures.

Previously, using comparable confocal parameters and 170-nsec-duration CO_2 -laser pulses, we were limited to an energy conversion efficiency of ~ 0.2 percent by laser-induced breakdown (LIB) effects in the liquid medium.¹³ By analogy with both gas- and solid-phase breakdown measurements, it was clear that using shorter-duration CO_2 -laser input pulses would result in an increased intensity threshold for the LIB process and a higher third-harmonic conversion efficiency. Using a single longitudinal mode CO_2 TEA laser oscillator-CdTe modulator- CO_2 TEA amplifier configuration, we have generated 8-nsec-duration CO_2 -laser pulses. We find that the LIB intensity threshold scales inversely as the square root of the laser pulse duration τ_p for pulse durations between 8 and 200 nsec and focal spot sizes of approximately $100 \mu\text{m}$ for all the cryogenic liquids we have investigated (CO , O_2 , N_2 , and Ar). For 8-nsec pulses and a spot size w_0 of $120 \mu\text{m}$, the LIB intensity threshold for liquid CO is approximately $3 \times 10^{10} \text{ W/cm}^2$. Details of the laser system and LIB measurements will be given elsewhere.¹⁵ This scaling law implies that the LIB limit to the THG efficiency is inversely proportional to τ_p .

With the double-pass geometry, using 8-nsec-duration CO_2 pulses and confocal parameters of approximately 1 cm, we have obtained a third-harmonic energy conversion efficiency of 4 percent. In a single-pass geometry, the THG efficiency in this experiment was 3.3 percent. Both of these efficiencies were limited by saturation effects; efficiencies in excess of 20 percent would have been achieved if the THG signal had increased as the third power of the input intensity up to the LIB threshold. The origin of this saturation behavior is presently not understood. We are undertaking an extensive experimental and theoretical program to evaluate the possible

mechanisms. In the present context, it is important to note that the use of the double-pass configuration results in an increase in the conversion efficiency, independent of this saturation behavior.

S. R. J. Brueck
H. Kildal

E. INVESTIGATION OF Hg_2^* AS A DISCHARGE-PUMPED OPTICAL STORAGE MEDIUM

High-pressure mercury vapor is known to possess several characteristics which make it attractive as a medium for an efficient, high-power laser in the near-ultraviolet. One of the most important of these characteristics is the collisional and radiative metastability of the lower molecular excimer states. Theoretical predictions as well as several recent kinetic studies have shown that in thermal equilibrium at reasonable temperatures nearly all the Hg_2 excimer population resides in the lowest lying 0_g^\pm excited states (see Fig. II-8). These are located several thousand wavenumbers below the upper state of the prospective laser transition $1_u \rightarrow 0_g^+(X)$ and are not coupled to the ground state by a single-photon radiative transition. We will describe below our progress on experiments designed to determine the feasibility of extracting the energy stored in the 0_g^\pm levels by means of an intense infrared pulse.

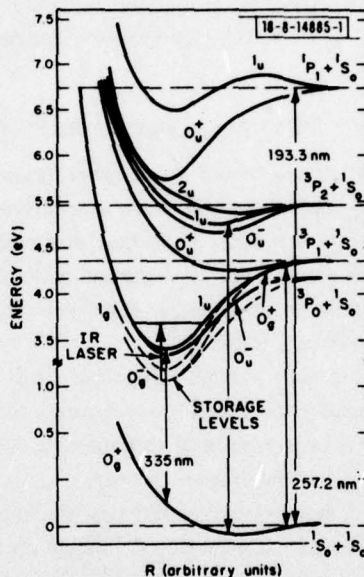


Fig. II-8. Hg_2 potential curves.

The energy stored in the 0_g^\pm storage states may be extracted by Raman or optical-pumping processes terminating in bound or free levels of the ground state, where the 1_u level acts as a virtual or real intermediate level. Calculation shows that among these processes, optical pumping possesses the highest gain per infrared flux. We have therefore begun with a characterization of this process.

Optical pumping of the $0_g^\pm \rightarrow 1_u$ transitions has been previously observed in both optically excited and discharge-excited mercury. However, in order to establish the potential of this process as a practical extraction technique, it is necessary to determine the absolute value of

the pumping cross section and the variation of this quantity with the infrared-pumping wavelength. It is also necessary to understand the kinetics of the relevant absorption and deactivation processes.

The infrared-pumping experiments were carried out with the multiline output of the HF, DF, and HBr lasers and with single lines of the HF and DF lasers. The efficiency of the optical pumping of the $0_g^{\pm} \rightarrow 1_u$ transitions was observed to be nearly independent of the infrared wavelength used. This means that in a practical extraction scheme, a multiline HF laser can be used. However, the induced ultraviolet spectrum for the $1_u \rightarrow 0_g^+(X)$ fluorescence showed a marked dependence on the infrared wavelength, indicating that a significant unrelaxed population of 1_u level exists. This allows the wavelength for gain in the mercury excimer system to be "tuned" over a limited range by choosing the infrared extraction wavelength.

There is no sign of saturation in the induced fluorescence with a multiline infrared laser flux of up to 7 MW/cm^2 . This indicates that influx into the specific storage levels does not limit the pump rate even at these intensities. Enhancements of greater than 10 in the integrated ultraviolet band have been observed. However, much larger enhancements at specific wavelengths were measured in the wings of the emission spectrum. The data have thus far been limited to atomic densities greater than $5 \times 10^{17} \text{ cm}^{-3}$. At these densities the pumped states are highly quenched. It is therefore important to extend these measurements to lower densities where the decay of the 1_u state will be radiatively limited.

D. J. Ehrlich
R. M. Osgood, Jr.

F. EFFICIENT THALLIUM PHOTODISSOCIATION LASER

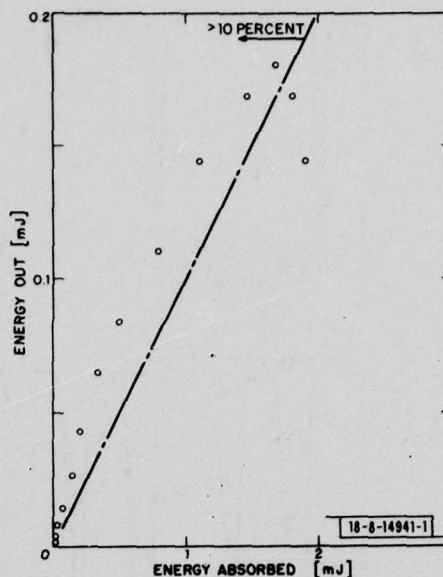
Lasers which are based on the photolysis of molecular species into electronically excited atomic or molecular fragments are attractive candidates for efficient high-energy gas-laser systems. This is a result of the fact that radiative dissociation can be very specific as to fragment excitation, and many such dissociative absorption bands are well matched in frequency and bandwidth to ultraviolet excimer sources. Despite this, photodissociative lasers have been inefficient (≤ 4 percent) to date.¹⁶

We describe here a highly efficient, viz 35-percent quantum efficiency and 14-percent energy efficiency, photodissociation laser which emits at either 535 or 378 nm, or both. In addition, we report on measurements of the output line profile of this laser which we have made with a scanning Fabry-Perot interferometer.

The laser operates by photolyzing thallium iodide (TlI) into the excited $\text{Tl } 7^2S_{1/2}$ state (along with unexcited I) with the 193-nm output of an ArF laser. Laser action occurs at the 535- and 378-nm wavelengths of the $7^2S_{1/2} \rightarrow 6^2P_{3/2}$ and $7^2S_{1/2} \rightarrow 6^2P_{1/2}$ transitions. TlI was selected because it is known to have a high quantum yield of dissociation into $\text{Tl } 7^2S_{1/2}$ near 200 nm (≈ 40 percent).¹⁷ Adequate vapor pressure of TlI was obtained by heating the salt contained in a 5-cm quartz cell in an oven to between 250° and 400°C. After each laser pulse, the dissociation fragments recombined on a time scale rapid compared with the 1-sec interpulse spacing.

Because of the large transition moment for both the visible and ultraviolet transitions, the laser operated in the superfluorescent mode. A measurement was made of the 535/378-nm power ratio as a function of the $\text{Tl } 7^2S_{1/2}$ density, and it was found to vary in a manner which was consistent with the relative stimulated-emission cross-section and saturation behaviors.

Fig. II-9. Energy conversion of 193-nm pump into total thallium laser output.



The results of measurements of the ArF to Tl laser conversion efficiency are shown in Fig. II-9. At inversion densities far above threshold, the conversion follows a slope efficiency of 14 ± 3 percent, corresponding to a quantum conversion close to that anticipated from the photodissociation quantum yield of the parent compound. At high absorbed energies, spatial nonuniformities in the Tl $7^2S_{1/2}$ distribution cause a reduction in the Tl laser output.

A previously unexplored, but nonetheless extremely interesting, aspect of atomic photodissociation lasers has been their linewidths. Since photolysis of a low-pressure medium leaves the excited photofragments in a collisionless environment, analysis of the resulting emission lineshape reveals details of the photodissociative mechanism. In our laser, at typical pressures the Tl $7^2S_{1/2}$ atom radiates before undergoing a collision; hence, the laser, Doppler-broadened linewidth should be characterized by a superthermal average velocity, which reflects the translational energy imparted to the Tl atom during dissociation. Preliminary measurements indicate this is true in our case. Figure II-10(a-d) shows a typical Fabry-Perot scan of the Tl green line at four different Tl pressures (and hence different 535-nm laser energies). The two widely spaced features result from laser emission from the two upper-state hyperfine levels. As may be seen, the laser may be made to lase from a single upper level by operating near threshold. We are currently investigating the source of the splitting in each line which increases with pressure or 535-nm laser energy.

D. J. Ehrlich
J. Maya†
R. M. Osgood, Jr.

† GTE Sylvania, Danvers, Massachusetts.

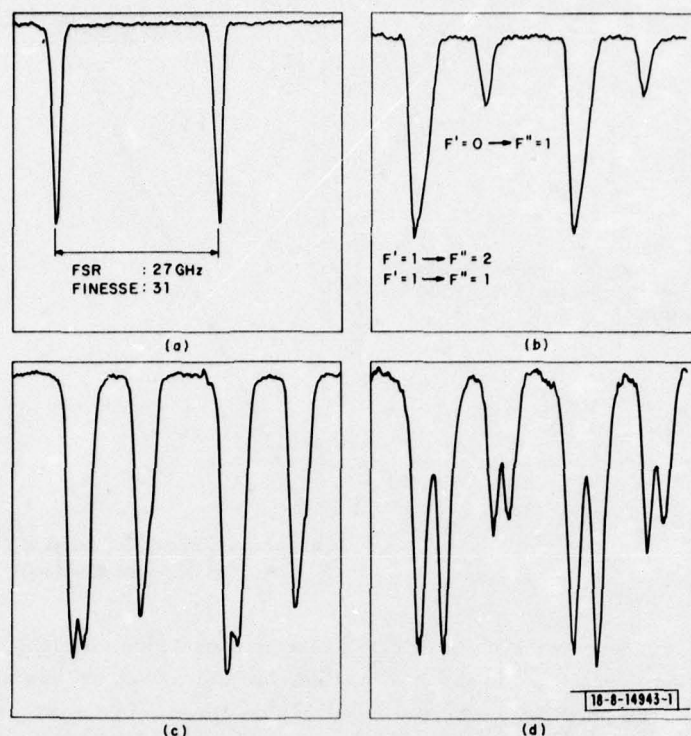


Fig. II-10. Fabry-Perot scans of 535-nm laser line vs increasing absorbed energy density. (a) $15 \mu\text{J}/\text{cm}^3$, (b) $40 \mu\text{J}/\text{cm}^3$, (c) $90 \mu\text{J}/\text{cm}^3$, and (d) $1300 \mu\text{J}/\text{cm}^3$. Fabry-Perot finesse is 31, free spectral range is 27 GHz.

G. REAL-TIME SPECTRAL ANALYSIS OF FAR-INFRARED-LASER PULSES USING A SAW DISPERSIVE DELAY LINE

High-power, optically pumped submillimeter lasers have recently been developed for use in plasma diagnostics. We report here a novel technique, using harmonic heterodyne detection in conjunction with a surface acoustic wave (SAW) dispersive delay line, to perform a real-time spectral analysis of the laser signal. In our initial experiments, we have resolved the contribution of three narrow longitudinal modes to a $385\text{-}\mu\text{m}$ D_2O laser's spectral linewidth. Furthermore, we have obtained confirmation that the mechanism of lasing is via a stimulated Raman process which tunes with a linear dependence on pump frequency.

Characterization of these high-power lasers has heretofore been particularly difficult since the repetition period of the 100-nsec laser pulses is typically from 1 to 10 sec. Because of the variability of the pulse behavior from shot-to-shot, all the desired frequency information must be obtained on one pulse. This last constraint effectively limits the useful role of high-finesse Fabry-Perot interferometers, which determine only average characteristics. A transient digitizer can, of course, be used with a computer capable of performing near-real-time Fourier transformation. However, use of a SAW dispersive delay device provides a simple method of obtaining real-time pulse spectral analysis in this type of experiment.

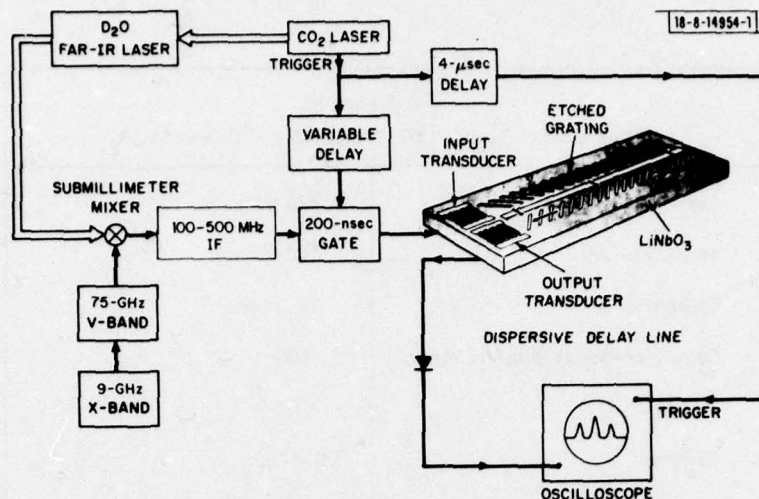


Fig.II-11. Experimental setup for pulsed heterodyne experiment. SAW device is used to perform a real-time spectral analysis of optically pumped D_2O submillimeter laser signal.

In pulse measurements that involve frequency analysis, the laser signal must first be heterodyned with a local oscillator to produce an IF which is then processed to provide the desired information. Figure II-11 is a diagram of the overall setup. In our experiment, we mix the submillimeter laser pulse at 779 GHz (385 μm) with the 11th harmonic of a tunable V-band klystron in a GaAs Schottky-diode mixer, producing an IF of 420 MHz. The mixer diode was of the planar, surface-oriented type used in an open mount. The signal then proceeds to the $LiNbO_3$ dispersive delay line and is displayed on a high-speed storage oscilloscope.

The essential concept for the present application is that frequency components lying within the 100-MHz bandwidth of the SAW device (also called a reflective-array compressor, or RAC) centered at 420 MHz will be delayed from 4 to 20.3 μsec with a linear dependence on frequency, a constant 4- μsec delay plus a dispersive delay of 16.3 μsec . The display on the scope then effectively becomes equivalent to that of a spectrum analyzer. The success of this technique relies strongly on the fact that the signal processing takes place subsequent to external electrical pickup noise. A variable 200-nsec gate further aids in minimizing the electrical noise by allowing signal input to the SAW device only while the 100-nsec laser pulse is on.

The RAC used as the frequency dispersive element was originally developed for use as a radar pulse expander and compressor with wide bandwidth and large compression ratio. The basic RAC configuration is shown as part of Fig.II-11. The input and output interdigital transducers convert an electrical signal to a Rayleigh SAW, and vice versa, respectively. The oblique grooves in this device have a spacing that increases as a function of distance from the input transducer. The surface wave is strongly reflected at a right angle at a point in the reflective array where the groove spacing in the propagation direction matches the wavelength of the surface wave. A second reflection in a symmetrically placed mirror-image grating sends the wave to the output transducer. The groove positions are established such that the surface wave travels from input to output along a path whose length (and group delay) is a linearly

TABLE II-1 PARAMETERS OF REFLECTIVE-ARRAY COMPRESSOR	
Center Frequency	420 MHz
Bandwidth Δf	100 MHz
Dispersion T	16.3 μsec
Dispersion-Bandwidth Product	1630
Constant Delay	4 μsec
Material	LiNbO_3
Insertion Loss	30 dB (flat across passband)

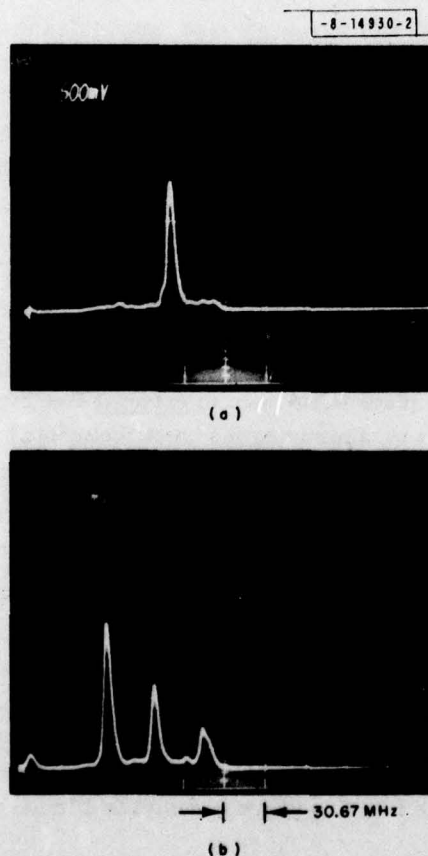


Fig. II-12. Oscilloscope display of output of SAW dispersive delay line: (a) shows, as a function of frequency, single-mode laser signal at low laser output powers; (b) displays three longitudinal modes, generated at high laser powers.

increasing function of frequency, a so-called up-chirp. The RAC used in the present experiment was conventional in design; its parameters are given in Table II-1.

The number of resolvable frequencies is proportional to $(T\Delta f)^{1/2}$, where the proportionality constant is of the order of unity and depends on the precise definition of the resolution. For the present case, the RAC device provides approximately 40 resolution elements or, equivalently, a resolution of about 2.5 MHz. In order to produce a nondeformed spectral image, the requirements $3/2\sqrt{T\Delta f} \leq T/\tau \leq T\Delta f/4$, where τ is the pulse duration, must be satisfied. For our case $\tau = 100$ nsec, so that $60 \leq 160 \leq 400$.

Figure II-12(a) shows the output of the delay line when heterodyning the harmonics of a V-band klystron with a single mode of a D_2O laser pulse from a relatively low-power (~ 200 -kW) submillimeter laser. The total linewidth is seen to be about 7.5 MHz and is quite reproducible. The 30.67-MHz coordinate axis derives from the 16.3- μ sec dispersion over a 100-MHz bandwidth. Figure II-12(b) shows the same laser operating at higher pump and higher output powers (~ 1 MW). Although every shot is somewhat different in amplitude distribution, we have been able to determine the presence of up to three narrow, adjacent longitudinal modes of the 4-m-long oscillator cavity. The frequency of the V-band was determined by mixing with a multiplied X-band stabilized reference to which it can also be locked. This has allowed the V-band to be tuned, the bandwidth of the measurement to be extended, and verification to be obtained that all the modes have been observed. The detection of these narrow modes is a particularly important result since Fabry-Perot studies had indicated that the high-gain D_2O lasing medium may be generating a broad spectral band several longitudinal modes wide.

At the highest pump levels, the 385- μ m D_2O laser is expected to be predominately a stimulated Raman process. In this regime of operation the submillimeter output frequency is a linear function of the CO_2 pump frequency. This has been observed in recent measurements¹⁸ using a Fabry-Perot interferometer and tuning the CO_2 with ZnSe etalon in steps of 112 MHz. Now, using the RAC device and tuning our local oscillator, we have been able to follow the submillimeter output continuously through several hundred megahertz. This represents a definitive determination that emission is by a stimulated Raman process, and indicates the potential of using this laser system as a source of continuously tunable high-power radiation.

We believe that this is the first time a SAW dispersive filter has been used to obtain a Fourier transform of a laser pulse for the purpose of studying a laser's spectral characteristics. The output of a dispersive delay line is actually the Fresnel transform of the input signal. If the time extent of the input signal falls within the limits discussed previously, the Fresnel transform is an adequate approximation of the Fourier transform. This condition holds in the present case; moreover, knowledge of the precise arrival time of the pulse allows exact determination of the frequency-vs-time relation. If these conditions are satisfied (as they are, in fact, in many pulsed-laser experiments), it is possible that this technique will find application in areas such as optical radar signal processing as well as in the spectral analysis of fast, time-dependent laser-related phenomena. An extension of this type of signal processing, the chirp transform, is more complex, but has a wider potential in other areas involving spectral analysis of fast, time-dependent phenomena.

H. R. Fetterman	R. C. Williamson
P. E. Tannenwald	P. Woskobochnikow†
C. D. Parker	H. C. Praddaude†
J. Melngailis	W. J. Mulligan†

† National Magnet Laboratory, M.I.T. (work supported by DOE).

REFERENCES

1. H. Kogelnik, E. P. Ippen, A. Dienes, and C. V. Shank, IEEE J. Quantum Electron. QE-8, 373 (1972).
2. Solid State Research Report, Lincoln Laboratory, M.I.T. (1977:4), p. 15, DDC AD-A052463/7.
3. G. W. Iseler, H. Kildal, and N. Menyuk, "Ternary Semiconductor Crystals for Nonlinear Optical Applications," in Ternary Compounds 1977, edited by G. D. Holah (The Institute of Physics, Bristol and London, 1977), pp. 73-88, DDC AD-A054566.
4. H. Kildal, R. F. Begley, M. M. Choy, and R. L. Byer, J. Opt. Soc. Am. 62, 1398 (1972).
5. D. S. Chemla, R. F. Begley, and R. L. Byer, IEEE J. Quantum Electron. QE-10, 71 (1974).
6. A. P. Sukhorukov and I. V. Tomov, Opt. Spektrosk. 28, 651 (1970).
7. H. Kildal, Air Force Materials Laboratory Technical Report AFML-TR-72-277, Air Force Systems Command, Wright-Patterson Air Force Base, Ohio (December 1972).
8. Solid State Research Report, Lincoln Laboratory, M.I.T. (1978:2), pp. 11-13.
9. H. Kildal and S. R. J. Brueck, Phys. Rev. Lett. 38, 347 (1977), DDC AD-A042238/6.
10. _____, Appl. Phys. Lett. 32, 173 (1978), DDC AD-A054069.
11. S. R. J. Brueck and H. Kildal, Opt. Lett. 2, 33 (1978), DDC AD-A054569.
12. H. Kildal and G. W. Iseler, Appl. Opt. 15, 3062 (1976), DDC AD-A046031/1.
13. S. R. J. Brueck and H. Kildal, Opt. Lett. 2, 33 (1978), and references therein.
14. J. M. Yarborough, J. Falk, and C. B. Hitz, Appl. Phys. Lett. 18, 70 (1971).
15. H. Kildal and S. R. J. Brueck (in preparation).
16. R. Burnham, Appl. Phys. Lett. 30, 132 (1977); E. Schimitschek, J. Celto, and J. Trias, Appl. Phys. Lett. 31, 608 (1977).
17. J. Maya, Appl. Phys. Lett. 32, 484 (1977).
18. P. Woskoboinikow, H. C. Praddaude, W. J. Mulligan, D. R. Cohn, and B. Lax, submitted to Applied Physics Letters.

III. MATERIALS RESEARCH

A. UTILIZATION OF Sn-DOPED In_2O_3 (ITO) FILMS IN FABRICATION OF GaAs SOLAR CELLS

In order to investigate the possibility of using ITO films in the fabrication of GaAs solar cells, we have developed a technique for the reproducible deposition of highly transparent, highly conducting ITO films by means of ion-beam sputtering. Two possible applications are under study: the utilization of ITO/GaAs heterojunctions to form charge-separation barriers, and the employment of ITO films to form a transparent ohmic contact to the upper n^+ -GaAs layer in shallow-homojunction cells. If either application proves feasible, the use of ITO films in polycrystalline cells would be particularly advantageous, since these films would provide an upper cell surface with much lower lateral resistance than polycrystalline GaAs, permitting the use of less-extensive metal grids for current collection.

We previously reported^{†,‡} a method for depositing high-quality ITO films by RF sputtering. However, RF sputtering generally produces a large amount of surface damage and sample heating. The new technique using ion-beam sputtering was developed to avoid these disadvantages. Deposition is carried out in a modified commercial sputtering system (see Fig. III-1) that has a substrate platform which can be rotated in order to insure uniform film thickness. In experiments using glass substrates, it was found that the electrical and optical properties of the films are extremely sensitive to the O_2 pressure (p_{O_2}) during deposition, as we had previously shown for the RF-sputtered films. By accurately controlling p_{O_2} , which is monitored with a residual gas analyzer, we can reproducibly obtain high-quality films at substrate temperatures below 100°C . For our deposition conditions, the optimum value of p_{O_2} is about 3×10^{-5} Torr (N_2 equivalent). Films prepared under these conditions have resistivities of 6 to $8 \times 10^{-4} \Omega\text{-cm}$ (with electron concentrations of about $3 \times 10^{20} \text{ cm}^{-3}$ and Hall mobilities of about $30 \text{ cm}^2 \text{ V}^{-1} \text{ sec}^{-1}$) and visible transmission greater than 80 percent. If p_{O_2} is less than the optimum value, the resistivity remains almost the same but the transmission decreases; if p_{O_2} is greater than the optimum value, the transmission does not change very much but the resistivity increases rapidly.

To investigate the barrier properties of ITO/GaAs heterojunctions, ITO films about 5000 \AA thick were deposited by ion-beam sputtering, using the optimum conditions described, on n^+ and p^+ single-crystal GaAs wafers and on n and p epitaxial GaAs layers grown by CVD on such wafers. The as-deposited films formed ohmic contacts to the n^+ wafers, which had carrier concentrations of 5×10^{18} and $8 \times 10^{18} \text{ cm}^{-3}$. Ohmic contacts to the p^+ wafers (concentration of $9 \times 10^{18} \text{ cm}^{-3}$) were obtained by annealing for 1 sec at 150°C in flowing N_2 . Poor barriers were formed by as-deposited films on n -layers (concentrations between 1×10^{16} and $5 \times 10^{17} \text{ cm}^{-3}$); the barrier height was increased slightly by annealing in N_2 at temperatures up to 400°C , but the open-circuit voltage V_{oc} remained below 0.2 V for solar cells fabricated with these heterojunctions. The best barriers so far have been obtained for ITO films on p -layers (concentrations of about $5 \times 10^{16} \text{ cm}^{-3}$). These barriers remain stable up to 200°C , but degrade at higher temperatures.

[†]J. C. C. Fan and J. B. Goodenough, *J. Appl. Phys.* **48**, 3524 (1977), DDC AD-A046983/3.

[‡]J. C. C. Fan, F. J. Bachner, and G. H. Foley, *Appl. Phys. Lett.* **31**, 773 (1977), DDC AD-A053923.

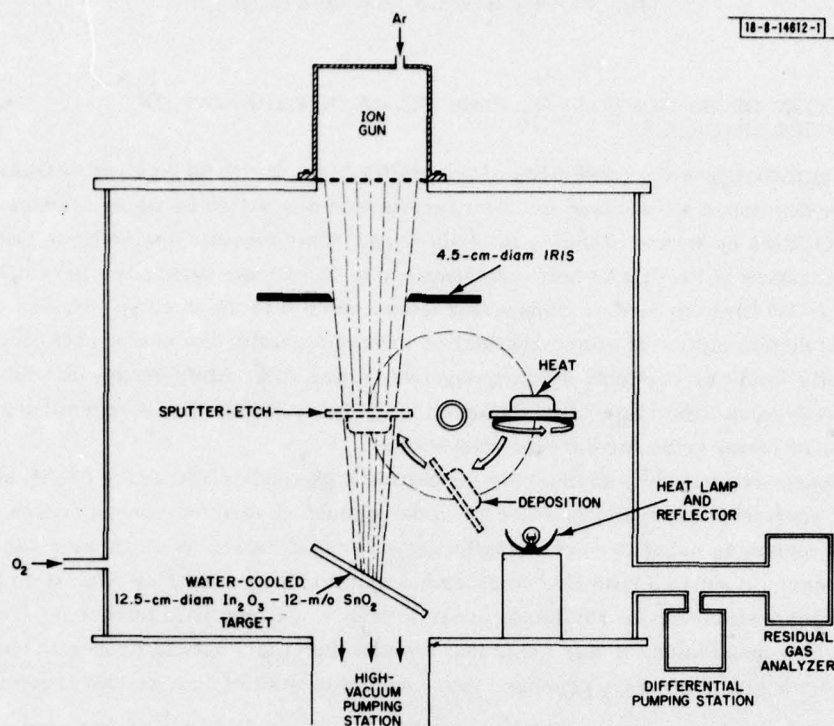


Fig. III-1. Schematic diagram of system for deposition of Sn-doped In_2O_3 (ITO) films by ion-beam sputtering.

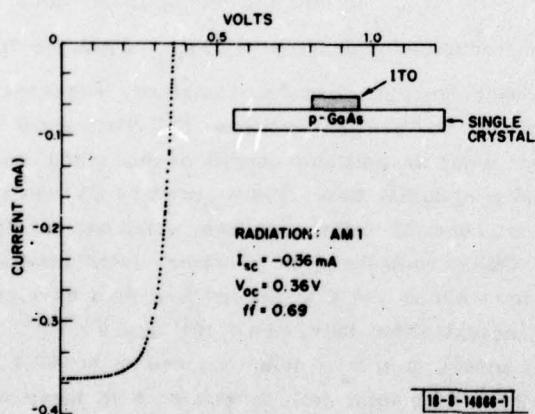


Fig. III-2. Current-voltage curve for a 1.5-mm-diam ITO/p-GaAs heterojunction cell.

Since ITO/p-GaAs heterojunctions were found to form the best charge-separation barriers, we have initiated the development of single-crystal GaAs solar cells utilizing such heterojunctions. So far, conversion efficiencies of about 5 percent at AM1 have been obtained for 1.5-mm-diam cells of this type. The short-circuit current density is quite high ($\sim 20 \text{ mA/cm}^2$), but V_{oc} is still quite low ($\sim 0.36 \text{ V}$). Figure III-2 shows the current-voltage characteristics of a typical cell under simulated AM1 illumination. Sputter-etching the GaAs surfaces before ITO deposition caused no significant change in the results.

Since ITO forms a good ohmic contact to n^+ GaAs, ITO films may be very useful for fabricating shallow-homojunction polycrystalline cells. For shallow-homojunction cells in which the metal fingers make direct contact with the upper GaAs surface, the higher lateral resistance due to grain boundaries in thin-film cells requires a larger number of metal fingers than in single-crystal cells. This increase in the number of fingers not only increases the contact shading area but can also lead to other detrimental effects, such as increased diffusion of metal down the grain boundaries, lowering V_{oc} .

As an alternative solution to the problem of lateral resistance in polycrystalline cells, ohmic contact to the upper, n^+ GaAs surface can be made with a transparent ITO film. Because the conductivity of ITO is lower than that of metals, a few metal fingers will still be needed, but these fingers will make contact with the ITO layer rather than to GaAs. Preliminary results on 1.5-mm polycrystalline GaAs shallow-homojunction cells utilizing ITO contacts have been encouraging. The homojunctions were formed by using vapor-phase epitaxy to grow a Zn-doped ($\sim 1 \times 10^{17} \text{ cm}^{-3}$) p-layer $2 \mu\text{m}$ thick, then an S-doped ($\sim 5 \times 10^{18} \text{ cm}^{-3}$) n^+ layer on large-grained p^+ wafers with crystallite dimensions up to about 1 mm. The thickness of the n^+ layers is not uniform since the GaAs growth rate varies greatly with crystallite orientation. Even those cells that include grain boundaries have quite high V_{oc} values. Figure III-3 shows the current-voltage characteristics of one of the better such cells under simulated AM1 illumination. The V_{oc} remains high, about 0.78 V, but the short-circuit current density is low, about 14.5 mA/cm^2 — giving an efficiency of about 8 percent. A possible cause of the low value of the short-circuit current density is that the n^+ layer may be too thick for efficient current collection.

J. C. C. Fan R. L. Chapman
C. O. Bozler F. M. Davis

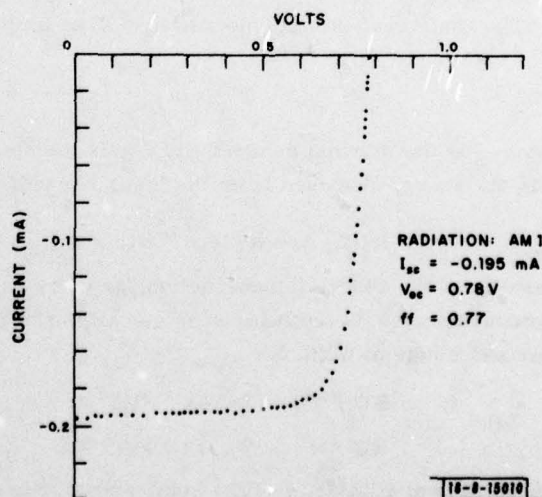


Fig. III-3. Current-voltage curve for a 1.5-mm-diam shallow-homojunction polycrystalline GaAs solar cell with contact made to upper GaAs surface by means of a transparent ITO film.

B. TEMPERATURE-PROFILE CALCULATIONS FOR A SEMICONDUCTOR HEATED BY A SCANNED CW LASER

To assist in the development of experimental techniques for using laser heating to crystallize semiconductor films and to anneal ion-implantation damage in semiconductors, a theoretical model has been developed for calculating the temperature profiles of semiconductor samples heated to temperatures below their melting points by scanning with the focused slit image of a laser.

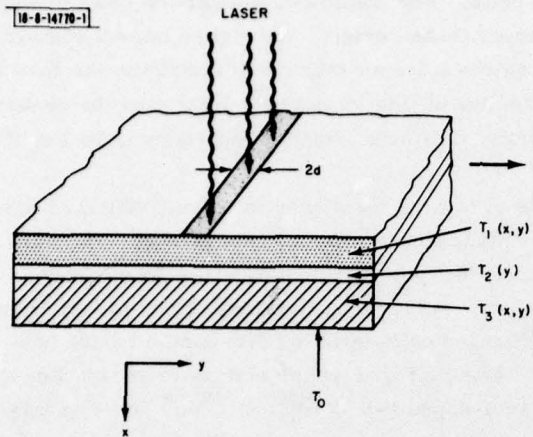


Fig. III-4. Schematic diagram of 3-layer structure assumed in temperature-profile calculations for a semiconductor heated by a scanned CW laser. Layers 1, 2, and 3 are, respectively, a semiconductor film, a thin coating, and a base.

For the case of laser crystallization, the structure treated consists of three layers, as shown schematically in Fig. III-4: a semiconductor film (layer 1) deposited on a thin coating (layer 2) on a relatively thick base (layer 3). The model assumes a laser beam slit image of uniform intensity, finite width, and infinite length that is laterally scanned across the semiconductor film, a coating so thin that there is no temperature difference across it, and a fixed temperature at the bottom of the base. The laser radiation absorbed in the semiconductor film is assumed to decrease exponentially with distance, and the radiation that arrives at the surface of the coating is assumed to be completely absorbed by the coating.

The basic heat flow problem to be solved in the semiconductor film is

$$\kappa_1 \nabla^2 T_1(x, y, t) - c_1 \rho_1 \frac{\partial T_1(x, y, t)}{\partial t} + H_1(x, y, t) = 0 \quad (\text{III-1})$$

where κ_1 is the thermal conductivity, c_1 is the specific heat per gram, ρ_1 is the density, and H_1 is the energy absorbed from the laser per unit volume. The term H_1 has the form:

$$H_1(x, y, t) = \alpha_1 J e^{-\alpha_1 x} \Theta(y + vt)$$

where α_1 is the absorption coefficient for laser radiation, J is the energy flux entering the semiconductor, v is the laser scan velocity, and $\Theta(y + vt)$ defines the shape of the scanning laser slit image of width $2d$:

$$\begin{aligned} \Theta(y + vt) &= 1 & |y + vt| < d \\ \Theta(y + vt) &= 0 & |y + vt| > d \end{aligned}$$

The latent heat of melting of the semiconductor is neglected in Eq. (III-1). Including the latent heat would make the problem analytically intractable.

For the steady state, $T_1 = T_1(x, y + vt)$, so that Eq. (III-1) becomes

$$\kappa_1 \nabla'^2 T_1(x, Y) - c_1 \rho_1 v \frac{\partial T_1(x, Y)}{\partial Y} + G_1(x) \mathfrak{D}(Y) = 0 \quad (\text{III-2})$$

where

$$Y \equiv y + vt, \quad G_1(x) = \alpha_1 J e^{-\alpha_1 x} \quad \text{and} \quad \nabla'^2 = \frac{\partial^2}{\partial x^2} + \frac{\partial^2}{\partial Y^2}.$$

The equations for the coating (layer 2) and the base (layer 3) are quite similar to Eq. (III-2), except that the x -dependence is dropped for layer 2, absorption of the laser radiation in layer 2 is assumed to be averaged over the coating, and no direct laser heating is included for layer 3.

The problem is solved by Fourier analysis of the temperature dependence in the Y -direction (along the layer) to yield, for layer 1, a differential equation of the form

$$\frac{\partial^2 \tau_1(x, k)}{\partial x^2} - \left(k^2 - \frac{c_1 \rho_1}{\kappa_1} i k \right) \tau_1(x, k) + \frac{G_1(x)}{\kappa_1} \frac{2 \sin kd}{k} = 0 \quad (\text{III-3})$$

where

$$\tau_1(x, k) = \int_{-\infty}^{\infty} T_1(x, Y) e^{ikY} dY$$

with similar equations for layers 2 and 3. The differential equations in the 3 layers have been solved with the following boundary conditions:

- (1) $\partial T_1 / \partial x = 0$ at the surface of layer 1 (negligible heat flow out of the surface).
- (2) $T_1(x, Y) = T_2(Y) = T_3(x, Y)$ at the values of x corresponding to the interface between layers 1 and 2 and the interface between layers 2 and 3 for all values of Y .
- (3) Net heat flow into layer 2 is zero in the steady state.
- (4) The temperature at the bottom of layer 3 is taken as the zero of temperature.

The solution for $T_1(x, Y)$ is then obtained by computing the inverse Fourier integral of $T_1(x, k)$. The terms in the resulting integrals along the real k -axis can be evaluated using contour integration in the complex plane by closing contours appropriately for three regions of Y :

$$-\infty < Y < -d, \quad -d < Y < d \quad \text{and} \quad d < Y < \infty.$$

The solution for $T_1(x, Y)$ consists of a convergent sum of contributions from the residues of the infinite number of poles of the integrands. One of the poles occurs at $k = 0$; the remaining poles occur for pure imaginary k values and must be located numerically.

A check on the correctness of the calculation is given by the requirement that the solutions, which look formally different in the three Y regions, must match numerically at the boundaries. This requirement is satisfied, but for some values of the parameters the contributions of up to 200 poles had to be included in order to obtain the match.

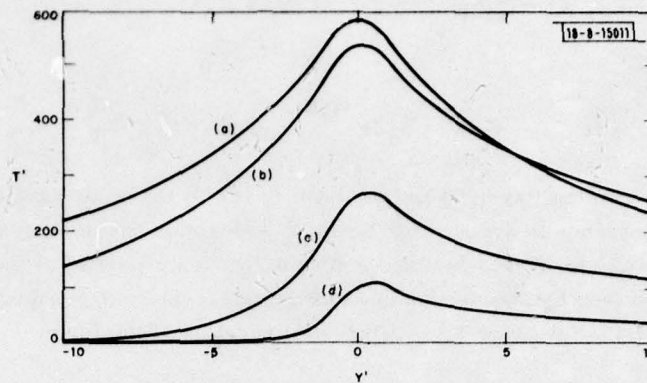


Fig. III-5. Calculated curves of normalized temperature T' as a function of normalized distance Y' along surface of GaAs film on Mo-coated glass base irradiated with scanned Nd:YAG laser, for thickness values given in text. Laser scan velocities are (a) 10^{-2} , (b) 10^{-1} , (c) 1, and (d) 10 cm/sec.

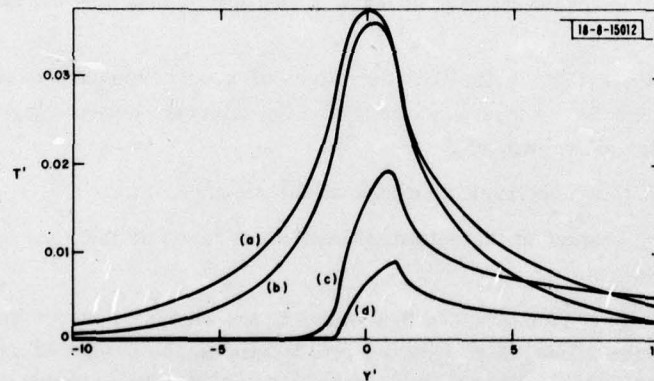


Fig. III-6. Calculated curves of normalized temperature T' as a function of normalized distance Y' along surface of 300- μm -thick GaAs sample irradiated with scanned Nd:YAG laser. Laser scan velocities are (a) 1, (b) 10, (c) 100, and (d) 500 cm/sec.

The above solution of the heat problem has been programmed for the IBM 370 computer and applied to a number of experimental situations. We shall first consider the laser crystallization of a GaAs film on metal-coated glass. For this case, the incident radiation is taken to be a slit image of the output of a Nd:YAG laser focused to a width of $100\text{ }\mu\text{m}$, the GaAs film is $2\text{ }\mu\text{m}$ thick, the metal coating is a Mo layer $0.5\text{ }\mu\text{m}$ thick, and the glass substrate is 1 mm thick. Figure III-5 shows plots of normalized temperature T' as a function of Y' , the distance in the plane from the center of the laser slit image, normalized to the laser image half-width d . The actual temperature is given by $T' (2L_1^2 J \alpha_1 / \kappa_1)$, where L_1 is the thickness of the GaAs film. The curves give T' at the upper surface of the GaAs ($x = 0$) for scan velocities of 10^{-2} , 10^{-1} , 1 , and 10 cm/sec . The T' curves for the bottom of the GaAs film are not perceptibly different from those for the top surface, while those for scan velocities less than 10^{-2} cm/sec are essentially the same as the one for $v = 0$. At a scan velocity of 10 cm/sec , the energy deposition front (on the left side of the temperature distribution in Fig. III-5) is moving faster than heat can diffuse, so that the leading edge of the thermal distribution sharpens.

We have applied the same basic model to the laser annealing of GaAs with a CW Nd:YAG laser by taking all three layers to be GaAs, with thicknesses of 50 , 0.5 , and $250\text{ }\mu\text{m}$, respectively. The dependence of T' at the upper surface on Y' is shown in Fig. III-6 for $v = 1$, 10 , 100 , and 500 cm/sec . The temperature profile for $v = 500\text{ cm/sec}$ (undoubtedly an impractical case) shows a striking sharpening of the leading edge.

H. J. Zeiger
B. J. Palm

IV. MICROELECTRONICS

A. CHARGE-COUPLED DEVICES: SAW/CCD BUFFER MEMORY

The first prototype of the SAW/CCD buffer memory^{1,2} has been tested, and preliminary electrical performance results have been obtained. The configuration of this SAW/CCD device is shown schematically in Fig. IV-1 and consists of a LiNbO_3 delay line in close proximity (typically 300 nm) to an array of 300 sampling fingers connected to a 300-stage CCD on a p-type silicon substrate. The piezoelectric fields associated with the SAW are sensed by the sampling fingers and used to modulate the charge in the signal wells. This charge is sampled, transferred to the 300-stage CCD shift register, and clocked out at a slow data rate.

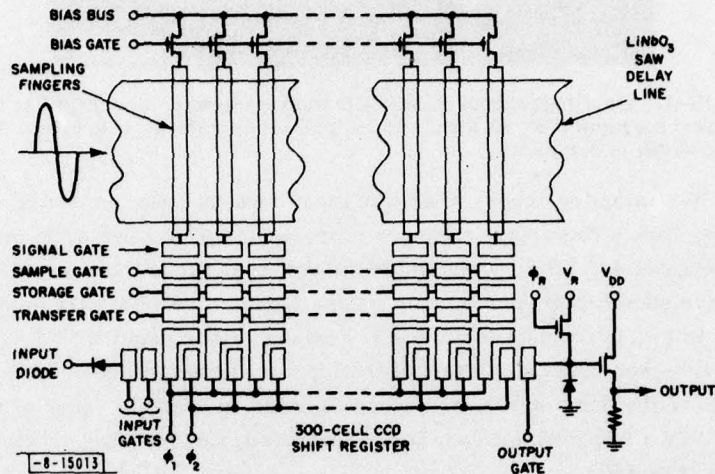


Fig. IV-1. Schematic diagram of acoustoelectric SAW/CCD buffer memory.

A prototype has been tested at a CCD clock rate of 100 kHz and at input signal frequencies between 80 and 130 MHz. From the sampling theory presented earlier,¹ one would expect frequency folding to occur at 85.7 and 128.6 MHz for a surface-wave velocity of 3480 m/sec and a finger spacing (spatial sampling period) of 40.6 μm . Frequency folding occurred in the prototype device at 85.6 and 128.3 MHz, within 300 kHz of these predicted values. One would expect the output-signal amplitude to be critically dependent upon the fall time of the 10-V negative-going step applied to close the sampling gate when the fall time approached the 5.6-nsec half-period of the input signal. In fact, this fall time could be varied from 1 to 10 nsec with no change in the output waveform. For slower edges, the output-signal amplitude dropped with increasing transition time, as one would expect. The reason that this transition can be so slow compared with the 5.6-nsec half-period of the input signal is the fact that the closing of the gate actually occurs over 1 V of the 10-V step, or in a time interval approximately one-tenth the total transition time.

Figure IV-2 is an example of the full 300-cell CCD output waveform at a CCD clock frequency of 100 kHz. The input signal is a 90-MHz sinusoid with a duration of 1.8 μsec at an input

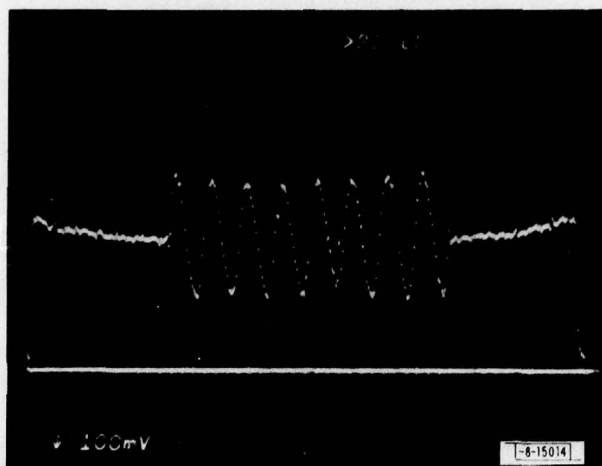


Fig. IV-2. Oscillograph of SAW/CCD buffer memory operation at input carrier frequency of 90 MHz and output clock rate of 100 kHz. Input pulse width is 1.8 μ sec.

power level of 2 W. Sampling occurs when this input burst is near the center of the interaction region of the delay line. This input frequency is translated by the sampling process to an effective output frequency of 4.3 MHz, which is the difference between the input of 90 MHz and the 85.7-MHz effective sampling frequency. As a result of this frequency translation, the sampled output waveform in Fig. IV-2 has $4.3 \times 1.8 = 7.7$ cycles rather than the $90 \times 1.8 = 162$ cycles contained in the 1.8- μ sec burst of 90 MHz at the input. The amplitude and phase of the output signal track those of the input signal, as expected. Also, a dynamic range of 25 dB has been observed, and with the implementation of a more sophisticated clocking scheme, a dynamic range of 40 dB is expected.

We have used successfully the acoustoelectric interaction between a piezoelectric surface wave and a silicon CCD to implement a fast-in, slow-out buffer-memory function. This compact solid-state device serves to store wideband analog signals and read them out at a slow data rate. Devices of this type promise to provide wideband analog buffer-memory functions for as many as 1000 discrete samples at input signal bandwidths up to 100 MHz or more. Electrical evaluation is continuing on this device and other samples in order to optimize the clocking waveforms and to find devices with fewer spot defects.

D. L. Smythe
R. W. Ralston
B. E. Burke

B. BINARY SYNTHETIC HOLOGRAMS

Two holographic masks consisting of arrays of rectangular apertures have been fabricated for the Opto-Radar Systems Group for use in an IR laser radar system. Within a hologram the minimum rectangular aperture size is on the order of $3 \times 45 \mu\text{m}$. The data file used to drive the pattern generator was created by using the Lee³ binary decision rule. Both holograms are designed to convert a uniform laser beam profile to a spherical wavefront, and, therefore, act as lenses.⁴ The two holograms differ by having different equivalent lens focal lengths. By studying the intensity distribution at the focal point, information will be obtained about the correctness of the computer coding technique, deviation from diffraction limited operation, resolution and

accuracy requirements of the masks, and noise characteristics. When these properties have been sufficiently determined, more complex beam shaping holograms will be fabricated.

Synthetic coding holograms³ consist of arrays of rectangular apertures built up from single-size, building-block rectangles, in our case nominally $3 \times 45 \mu\text{m}$. This rectangle size is also the minimum-size aperture in the hologram. The areas of the apertures are proportional to the amplitudes of the wavefront as calculated at the corresponding sampling locations in the hologram plane. The positions of the apertures are shifted from the center of the sampling interval by an amount proportional to the phase of the wavefront at the corresponding sampling locations in the hologram plane. The general problem of making binary synthetic holograms is to find a function, $h(x,y)$, that has 0 or 1 as its value and can produce any desired wavefront by changing its parameters. As a result of collaborative efforts with the Opto-Radar Systems Group, software has been developed to make their programs compatible with the D.W. Mann pattern generator.

Fig. IV-3. Test binary hologram mask acting as a synthetic lens. Hologram is $4 \times 4 \text{ mm}$ and is constructed of 17,144 $2.5 \times 45.7 \mu\text{m}$ minimum-size rectangles. Coding scheme is designed for a mask of 75-percent transparency. Illustration is blowup of reverse-polarity 10X reticle for this mask, which indicates character of hologram with minimum of photographic distortion.

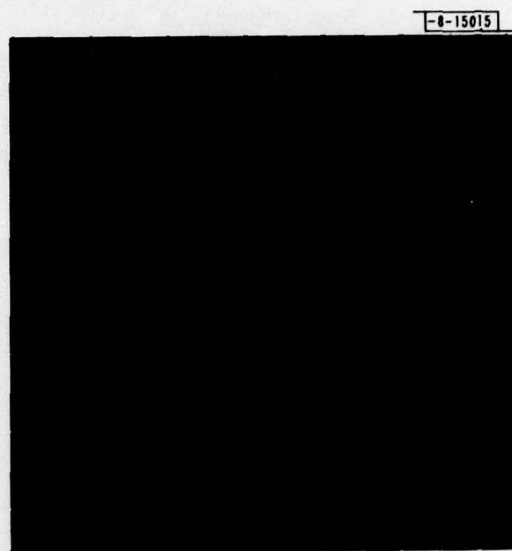


Figure IV-3 shows a test hologram acting as a synthetic lens. The hologram pattern was initially generated at 10X magnification on a Kodak emulsion plate using a D.W. Mann 1600A pattern generator. The building-block rectangle size was 1×18 mils on the 10X reticle, and the hologram was built up using this size block. The first hologram, which covered an area $4 \times 4 \text{ mm}$, was designed for 75-percent transparency, and required 17,144 exposures with a running time of 16 hr. The second hologram, which was $6 \times 6 \text{ mm}$, was designed for 50-percent transparency, and required 30,101 exposures with a 24-hr running time.

The excessive running time results from the slow speed of the 1600A pattern generator and from the problem of overfracturing. Overfracturing refers to the makeup of the pattern, which is the hologram, by single-size rectangles. For conventional pattern-generator work, IBM 370 software is available to fracture large patterns into various-size rectangles from 6 to $3050 \mu\text{m}$ in either X or Y. However, the Lee coding technique, utilizing a single-size rectangle as a building block, requires more pattern-generator running time than the optimum set of various-size rectangles which could be used to generate the pattern. This problem could be resolved by a software pattern-merge program, and re-sorting using our IBM 370 program. The merge

program would be rather difficult to write, however, and a search is being made to find such a program outside the Laboratory.

The final 1X mask is fabricated on a 10X-reduction photorepeater using 2- \times 2-in. chromium-coated mask plates with 900 Å of AZ 1350 positive-working photoresist on 1200-Å chromium.⁵ Tests of holograms generated by contact exposure from these masks are in progress.

D. J. Silversmith
G. L. Durant
H. H. Pichler

REFERENCES

1. Solid State Research Report, Lincoln Laboratory, M.I.T. (1977:4), pp. 37-39, DDC AD-A052463/7.
2. Ibid. (1978:2), pp. 35-36.
3. W-M. Lee, Appl. Opt. 13, 1677 (1974).
4. A. W. Lohman and D. P. Paris, Appl. Opt. 6, 1567 (1967).
5. Solid State Research Report, Lincoln Laboratory, M.I.T. (1977:3), p. 39, DDC AD-A050551/4.

V. SURFACE-WAVE TECHNOLOGY

A. AUTOMATED PULSED TECHNIQUE FOR MEASURING PHASE AND AMPLITUDE RESPONSE OF SAW DEVICES

An automated pulsed technique has been developed for measuring the phase and amplitude response of SAW devices. Because of the long delays (up to 10^5 periods) and need for precise phase response often encountered in SAW devices, particularly stringent demands are placed on the measurement system. This is especially true in the case of the large time-bandwidth-product dispersive delay lines for which the measurement system was originally developed.¹⁻³

Pulsed operation provides a number of advantages not available in conventional CW network analyzers. In order to determine the characteristics of the delayed SAW signal by means of a CW network analyzer, it is usually necessary to suppress direct electromagnetic feedthrough to a level about 40 dB below the delayed SAW signal. By operating in a pulsed mode, phase and amplitude measurements can be made in the presence of large feedthrough. This feature is particularly useful in evaluating preliminary devices because elaborate packaging to reduce feedthrough is not required. Pulsed operation also makes possible the measurement of the response for each discrete tap of a device in which the outputs of several taps are internally summed. This feature was essential during the development of a burst matched filter.⁴ The repetition rate is adjusted so that the next input pulse occurs after all signals from the previous pulse have died away. When desired, the input pulse can be lengthened to measure an effectively CW response which includes all spurious signals in the device.

Computer control of the measurement system makes possible the rapid accumulation, analysis, and display of data. The time-bandwidth product for a SAW device is a measure of the number of cycles of phase change which occur over the bandwidth of the device. For devices with time-bandwidth products of approximately 10^4 , a meaningful display of the phase response requires some type of curve fitting, a procedure straightforwardly handled by a computer. Computer control also allows for rapid and frequent system calibration, which results in precise measurements.

1. Measurement of Phase Response

A simplified schematic of the system used for measuring the phase of SAW devices is shown in Fig. V-1. In many SAW devices, a shift in frequency of only one part in 10^7 could cause a 1° shift in the output phase. For this reason, a precise, tunable frequency source, i.e., a frequency synthesizer, is employed in these measurements. A computer command sets the frequency of the CW signal from the frequency synthesizer. This signal is gated by an RF switch and applied to the device. The output from the device is mixed with a coherent reference signal and the resulting video is sampled. The integration of many samples enhances the signal-to-noise ratio. The integrated signal is A/D converted and put into the computer.

The duration of the RF pulse which excites the device is chosen so that the pulse is long enough to reach effectively CW conditions for the delayed SAW signal, but is also short enough to time-resolve direct, triple-transit, and feedthrough signals. The waveforms associated with a typical measurement are illustrated in Fig. V-2. The traces from top to bottom show the RF pulse applied to the device, the filtered video output from the mixer, the sampling gate for the delayed SAW signal, and the baseline sampling gate. The length and position of the sampling

gate for the SAW signal are adjusted so that the sampling occurs in the interval between the end of the direct feedthrough and the beginning of the turn-off transient. In order to compensate for DC drifts in the system and to allow AC coupling to video output from the mixer, a sample of the baseline is also taken. The baseline sampling gate is positioned in a portion of the video output where the acoustically generated signals and RF feedthrough are absent.

The phase response is determined by a π -point method, i.e., the frequencies at which the delayed SAW signal and the reference are in quadrature at the mixer are determined. In this case, the video output from the mixer is zero over the duration of the delayed SAW pulse. Since each successive π point indicates a phase shift of π radians, the measurement of the frequency at each π point is a direct determination of the phase response.

Speed, efficiency, and precision of the measurement are enhanced through the use of a highly interactive computer-controlled algorithm for data collection. To begin the measurement process, two successive π points are found by sweeping with a user-specified frequency increment. Since a typical SAW device closely follows a prescribed phase response, the frequencies of adjacent π points can be estimated by an appropriate extrapolation from the previously measured π points. For a nominally nondispersive device, the extrapolation is linear, whereas for a linear-FM dispersive device, the extrapolation is quadratic. On the basis of the extrapolation, the frequency of the synthesizer is set to that estimated for the next desired π point, and the value of the output voltage for the system is measured to determine whether the estimated frequency is too high or low. The frequency is then incremented until the π point is bracketed, and then the π -point frequency is calculated by interpolation from the values of the output voltages. This algorithm avoids a lengthy search for the frequencies corresponding to each π point.

Typically 100 π points at approximately equispaced frequencies are measured, all others being skipped over. This method avoids the potentially time-consuming task of sweeping through the entire test band to find all π points. Moreover, it decreases computer-processing and storage requirements. Also, since a file of π -point number vs frequency is maintained by computer, phase ambiguities are eliminated, even for devices whose phase varies by several thousand periods over the band of interest.

Calibration is also performed by computer. The phase response of the system is determined by replacing the device with a pad and repeating the phase measurement. The phase response is stored in a file and subtracted from the phase response measured with the device in the system. In order to measure the system response, a delay line consisting of a long cable is permanently placed just before the RF switch. The length of this cable is made several times as long as the inverse of the frequency span over which measurements are to be made. This ensures that several π points are obtained during measurement of the system response. This computer-aided calibration has increased the accuracy of the system to better than 0.5%.

The computer also fits a curve to the data and plots the deviation from ideal. A typical result is shown in Fig. V-3. In the case of a reflective-array-compressor¹⁻³ (RAC) device, the data are stored and later used to generate a computer-designed pattern of metal which is deposited between the two gratings of the RAC in order to modify the phase response and minimize the deviations from the desired ideal response.

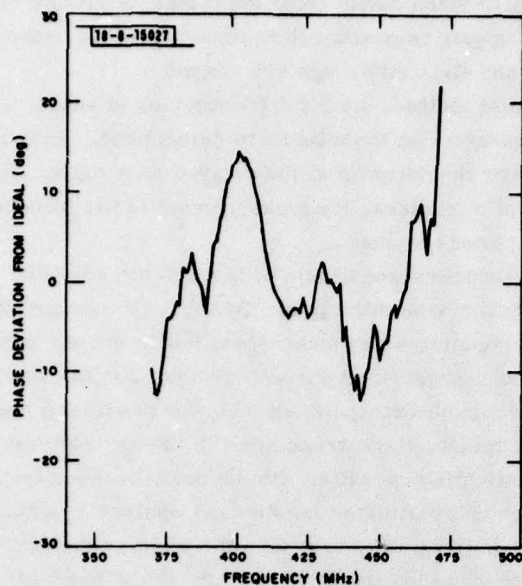


Fig. V-3. Example of measured phase response for SAW device. In this case, device is dispersive and ideal phase response is quadratic.

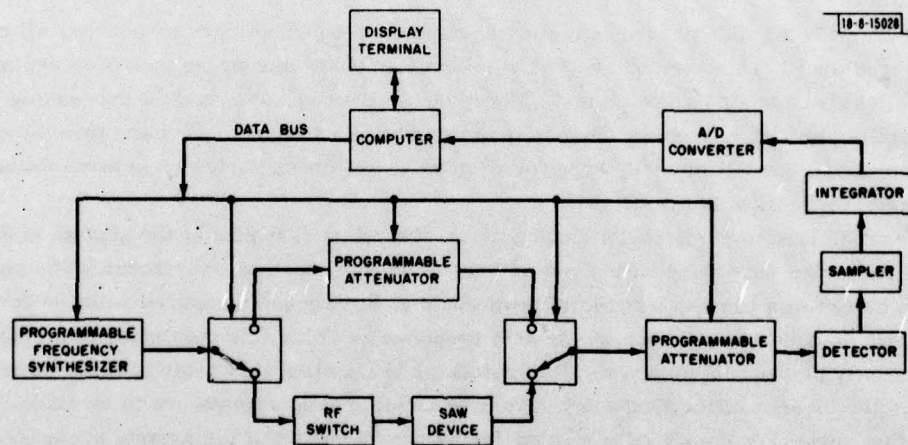


Fig. V-4. Schematic diagram of system used to measure insertion loss of SAW devices. Several amplifiers, pads, and filters employed in system are not shown.

2. Measurement of Insertion Loss

Figure V-4 illustrates the system used to measure the insertion loss of SAW devices by a substitution method. An RF pulse is applied to the device, and the delayed SAW signal at the output is detected, sampled, integrated, and input to a computer. Then, the computer substitutes a programmable attenuator for the branch of the system containing the device, and adjusts the attenuator to give an output signal which closely matches that obtained for the branch containing the device. Because the attenuator steps are discrete, computer interpolation is employed to further refine the measurement of insertion loss. The attenuator just before the detector is adjusted by the computer to keep the signal level into the detection circuit within its dynamic range.

Calibration of the system is achieved by replacing the device under test with a calibrated attenuator and measuring the insertion loss of the branch of the circuit containing the attenuator, RF switch, and associated amplifiers. The difference between this measured loss and the attenuation of the calibrated attenuator is saved in a file. These corrections are subtracted from the value of the loss of the same portion of the circuit measured with the device in place. By this method, the magnitude of the insertion loss of the device is measured to a repeatability of 0.2 dB over a range up to 120 dB. The ultimate accuracy is directly related to the calibration of the fixed and programmable attenuators. The results for a typical measurement of insertion loss are shown in Fig. V-5.

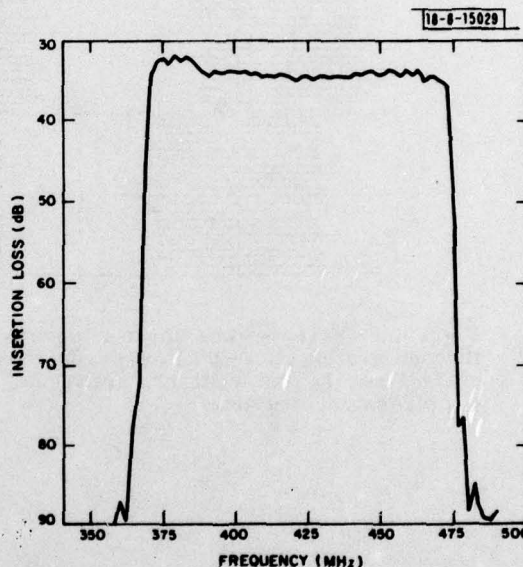
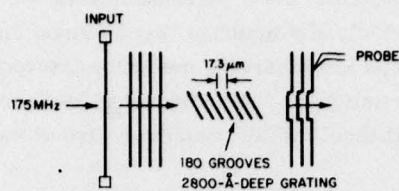


Fig. V-5. Example of measured insertion loss for SAW device.

Finally, processed data are displayed on a storage scope and may be stored for later use in transducer and grating redesign. Comparison of measured and ideal responses is easily done by computer, the results being displayed in a variety of formats.

J. H. Holtham
R. C. Williamson



18-8-15030

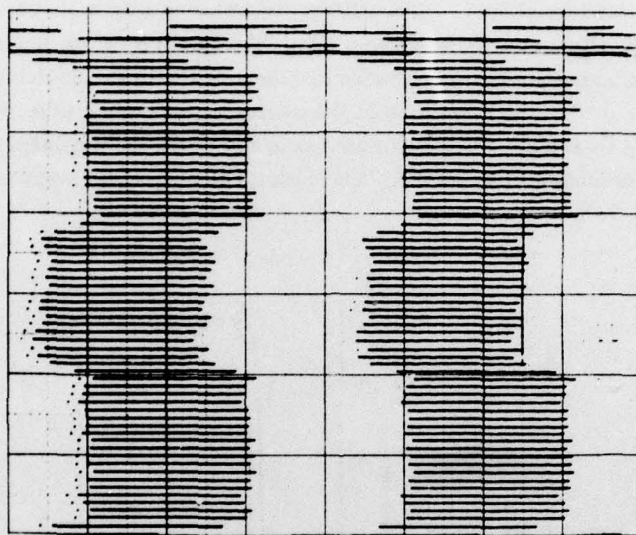


Fig. V-6. Surface-probe image of surface wave front after it has passed through grating on Y-Z LiNbO_3 . Width of grating spans approximately central one-third of width of wave front. Grooves are at angle of 46.81° to propagation direction.

B. SAW PHASE SHIFTS DUE TO PROPAGATION IN SHALLOW-GROOVE GRATINGS

In the design and fabrication of RAC devices,¹⁻⁴ one of the most difficult goals is accurately obtaining the phase response corresponding to a linear chirp. A linear chirp implies a phase response which is a quadratic function of frequency. The permitted deviations of the phase response from ideal quadratic is often only a few degrees. Since the propagation delay in RAC devices may be as long as 10^5 periods, the precise control of the delay to a few parts in 10^7 is needed.

The three main effects which frustrate attempts to achieve precise control of phase response are:

- (1) Variations in velocity within a sample or from sample-to-sample.⁵
The latter variations are typically ± 0.1 percent in LiNbO_3 .
- (2) Variations in the dispersion from sample-to-sample.⁶ The dispersion is characterized by a frequency-dependent velocity $v = v_0 (1 - bf)$. Values of b between $0.24 \times 10^{-3} \text{ GHz}^{-1}$ and $1.24 \times 10^{-3} \text{ GHz}^{-1}$ have been reported for LiNbO_3 (see Ref. 6).
- (3) The phase shift or slowing of the surface wave produced by propagation through gratings.^{1,7}

All three effects can produce phase shifts far in excess of the permitted limits. The first two effects are related to material growth and surface preparation, which need to be carefully controlled. The phase shifts due to the grooves can be corrected in the design of the reflective-grating mask,⁷ provided the phase shift per groove as a function of groove depth is known. The goal of this work is a determination of that relationship.

An existing model⁸ predicts that the phase shift per groove is proportional to the square of the groove depth, and is simply related to the imaginary part of the reflection coefficient. The model employs a single parameter C' to characterize the magnitude of all the shifts discussed herein. The imaginary part of the reflection coefficient has been measured by determining the magnitude of the reflection coefficient at the stop band, which is located near twice the frequency of the fundamental stop band. These measurements have been carried out for both normal-incidence⁸ gratings and oblique-incidence⁹ gratings on Y-Z LiNbO_3 . Here we report direct measurements of the phase shifts upon transmission through several types of gratings. The shifts are measured by observing the slowing of a wave propagating through a grating, and by observing the shift of the fundamental stop-band frequency of the gratings.

The relative slowing of the wave was measured by launching a surface wave with a beam about three times as wide as the grating upon which the wave impinges. The wave front behind the grating is somewhat retarded relative to the waves on the unperturbed surface, as shown in Fig. V-6. This retardation or phase shift can be observed directly with an electrostatic surface probe,¹⁰ as shown in Fig. V-6, or by specially placed transducers, as shown in the inserts of Figs. V-7 to V-10.

The results for normal-incidence gratings are shown in Figs. V-7 and V-8. The phase shift (Fig. V-7) and the frequency shift of the fundamental grating stop band (Fig. V-8) are both expected to be proportional to the square of the groove depth. A value of the proportionality coefficient $C' = 12.6 \pm 1.5$ fits the present results. Previous measurements of the imaginary

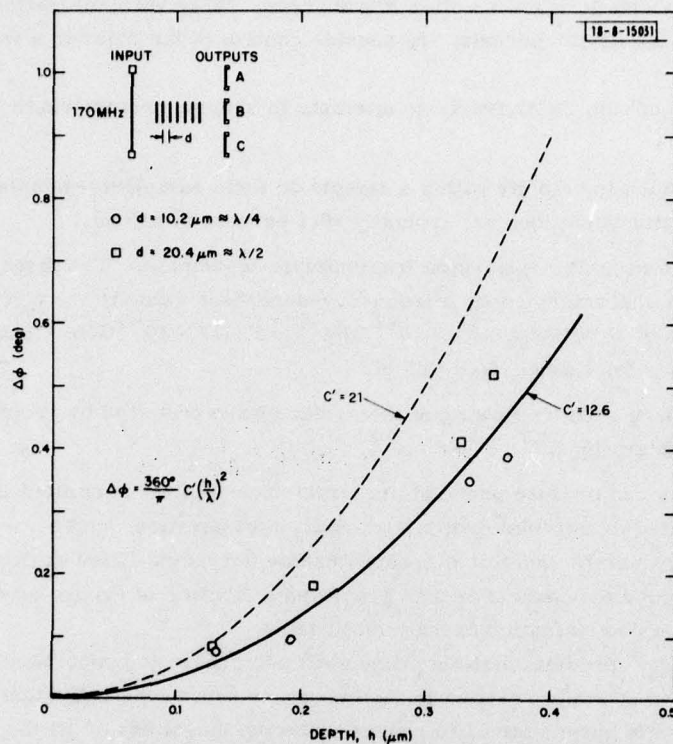


Fig. V-7. Phase shift per groove $\Delta\phi$ plotted vs groove depth for normal-incidence gratings. Solid line is quadratic fit to data with coefficient $C' = 12.6$. Dashed line is quadratic that would be predicted using coefficient deduced from previous measurements of imaginary part of reflection coefficient. Inset shows experimental layout. There are 200 grooves in each grating. Experimental data are taken by measuring difference between phase shift from input to B, and average of phase shifts from input to A and input to C.

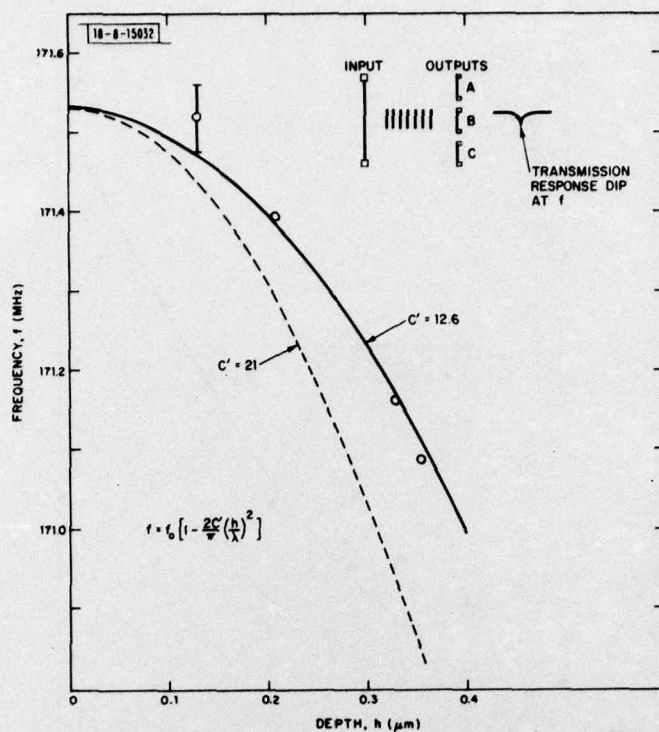


Fig. V-8. Frequency of fundamental stop band as determined from transmission-response dip plotted vs groove depth. Grating period $\sim \lambda/4$. Because of uncertainty in surface-wave velocity in Y-Z LiNbO₃, vertical placement of parabolic fitted curves (i.e., f_0) is somewhat arbitrary.

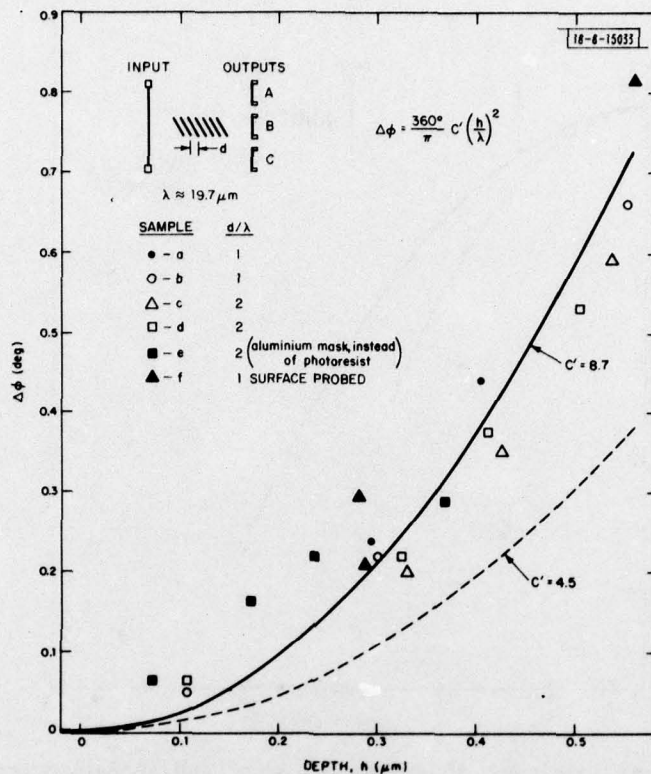


Fig. V-9. Phase shift $\Delta\phi$ per oblique-incidence groove plotted vs groove depth at frequency of 170 MHz. Solid line is quadratic fit to data with coefficient $C' = 7.6$. Dashed line is same plot using coefficient deduced from previous measurements of imaginary part of reflection coefficient. 10- μm -period gratings have 200 grooves, while 20- μm -period gratings have 100 grooves. Measurement technique is same as for Fig. V-7. Grooves are at angle of 46.81° to direction of incidence.

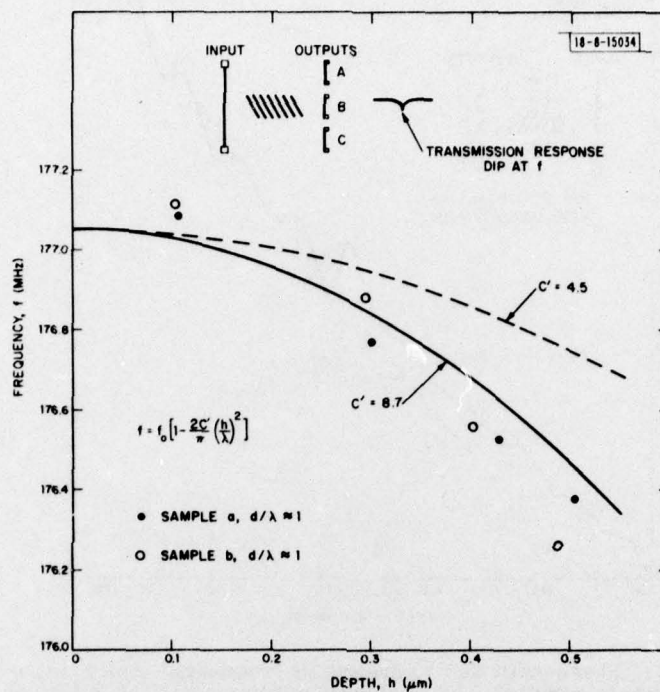


Fig. V-10. Frequency of transmission stop band plotted vs groove depth. Two candidate parabolic fits to data are shown.

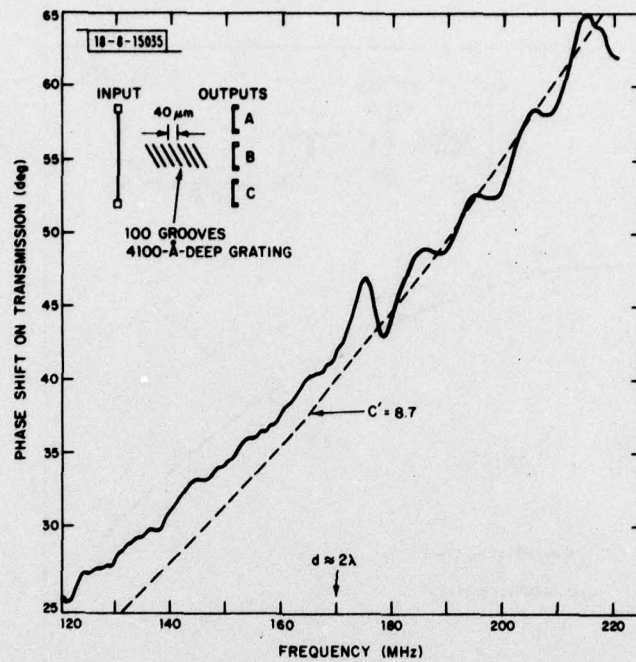


Fig. V-11. Phase shift due to grating vs frequency. Solid line is plot of computer-controlled phase-bridge measurement of difference of phase response from input to B, and average of responses from input to A and input to C. Ripples near 173 MHz are due to stop band in grating; other wiggles are due to interfering spurious signals. Dashed line is calculated using $C' = 8.7$ in equation given in Fig. V-9.

part of the reflection coefficient⁸ were fitted by a curve with a coefficient $C' = 21$. A value of $C' = 21$ was also consistent⁸ with earlier measurements of the shift on the frequency of the fundamental stop band for 100-groove normal-incidence gratings.¹ However, the experimental uncertainty of the measurements was so large that $C' = 12.6$ could also fit the data. The current measurements of frequency shift and phase shift significantly reduce the uncertainty in C' and indicate a disagreement with the measurements of the imaginary part of reflection coefficient, which appears to be outside of the combined experimental uncertainties.

The current measurements were made for two different grating periodicities. In one case, the grating period is approximately equal to a half-wavelength of the test wave, and the measurements examine the response near the fundamental stop band. In a coarser grating, the period is approximately equal to a wavelength, and the measurements characterize the response near twice the fundamental stop band. The measurements indicate that the phase shifts in the coarser grating appear to be slightly higher than the phase shifts in the finer grating. The frequency shift of the stop band near twice the fundamental stop-band frequency cannot be determined for these coarser gratings because of interfering bulk-wave effects.

In the oblique-incidence case (Figs. V-9 and V-10), there is also a disagreement between the previous measurements of the imaginary part of the reflection coefficient⁹ and the present transmission measurements, but in the opposite sense. The proportionality coefficient C' has to be approximately 4.5 to fit the measurements of the imaginary part, but a value of 8.7 is more consistent with the transmission and stop-band frequency-shift results.

A further set of measurements has determined the phase shift on transmission as a function of frequency for fixed depth. These measurements are also consistent with a value of $C' = 8.7$, as shown in Fig. V-11.

In summary, four different measurements have been performed: (1) measurement of the shift in frequency of the fundamental stop band as a function of groove depth; (2) measurement of the phase shift on transmission as a function of groove depth; (3) measurement of the phase shift on transmission as a function of frequency; and (4) measurement of the imaginary part of the reflection coefficient as a function of groove depth. The first three types of measurements are generally consistent with each other and indicate a value of C' which does not fit the results of the fourth type of measurement that had been performed earlier.^{8,9} This indicates that the stored-energy model^{8,9} does not account for the detailed behavior of surface waves in gratings. Nevertheless, the measurements taken so far are consistent with a quadratic dependence of phase shift on depth and on frequency, as predicted by the expression

$$\Delta\varphi = \frac{360^\circ}{\pi} C' \left(\frac{h}{\lambda}\right)^2$$

These measurements are useful in the design of the phase response of RAC devices and other surface-wave grating devices.

J. Melngailis

REFERENCES

1. R. C. Williamson and H. I. Smith, IEEE Trans. Microwave Theory Tech. MTT-21, 195 (1973), DDC AD-772211/9.
2. R. C. Williamson, V. S. Dolat, and H. I. Smith, "L-Band Reflective-Array Compressor with a Compression Ratio of 5120," in 1973 Ultrasonics Symposium Proceedings (IEEE, New York, 1973), pp. 490-493, DDC AD-A000498/6.
3. R. C. Williamson, Proc. IEEE 64, 702 (1976), DDC AD-A028461/2.
4. R. C. Williamson, J. Melngailis, and V. S. Dolat, "Reflective-Array Matched Filter for a 16-Pulse Radar Burst," in 1975 Ultrasonics Symposium Proceedings (IEEE, New York, 1975), pp. 400-404, DDC AD-A031718/0.
5. R. C. Williamson, "Measurement of the Propagation Characteristics of Surface and Bulk Waves in LiNbO_3 ," in 1972 Ultrasonics Symposium Proceedings (IEEE, New York, 1972), pp. 323-327, DDC AD-758935.
6. R. C. Williamson, "Problems Encountered in High-Frequency Surface-Wave Devices," in 1974 Ultrasonics Symposium Proceedings (IEEE, New York, 1974), pp. 321-328, DDC AD-A011322/5.
7. J. Melngailis, R. C. Williamson, J. H. Holtham, and R. C. M. Li, Wave Electronics 2, 177 (1976).
8. R. C. M. Li and J. Melngailis, IEEE Trans. Sonics Ultrason. SU-22, 189 (1975), DDC AD-A016700/7.
9. J. Melngailis and R. C. M. Li, "Measurement of Impedance Mismatch and Stored Energy for Right-Angle Reflection of Rayleigh Waves from Grooves in Y-Cut LiNbO_3 ," in 1975 Ultrasonics Symposium Proceedings (IEEE, New York, 1975), pp. 426-429, DDC AD-A031714/9.
10. R. C. Williamson, IEEE Trans. Sonics Ultrason. SU-19, 436 (1972), DDC AD-752971.

UNCLASSIFIED

SECURITY CLASSIFICATION OF THIS PAGE (When Data Entered)

REPORT DOCUMENTATION PAGE		READ INSTRUCTIONS BEFORE COMPLETING FORM												
1. REPORT NUMBER ESD-TR-78-245	2. GOVT ACCESSION NO.	3. RECIPIENT'S CATALOG NUMBER												
4. TITLE (and Subtitle) Solid State Research, 1978: 3.	5. TYPE OF REPORT & PERIOD COVERED Quarterly Technical Summary 1 May - 31 July 1978	6. PERFORMING ORG. REPORT NUMBER												
7. AUTHOR(s) Alan L. McWhorter	8. CONTRACT OR GRANT NUMBER(s) F19628-78-C-0002													
9. PERFORMING ORGANIZATION NAME AND ADDRESS Lincoln Laboratory, M.I.T. P.O. Box 73 Lexington, MA 02173	10. PROGRAM ELEMENT, PROJECT, TASK AREA & WORK UNIT NUMBERS Program Element No. 65705F Project No. 649L													
11. CONTROLLING OFFICE NAME AND ADDRESS Air Force Systems Command, USAF Andrews AFB Washington, DC 20331	12. REPORT DATE 15 August 1978	13. NUMBER OF PAGES 68												
14. MONITORING AGENCY NAME & ADDRESS (if different from Controlling Office) Electronic Systems Division Hanscom AFB Bedford, MA 01731	15. SECURITY CLASS. (of this report) Unclassified	15a. DECLASSIFICATION DOWNGRADING SCHEDULE												
16. DISTRIBUTION STATEMENT (of this Report) Approved for public release; distribution unlimited.														
17. DISTRIBUTION STATEMENT (of the abstract entered in Block 20, if different from Report)														
18. SUPPLEMENTARY NOTES None														
19. KEY WORDS (Continue on reverse side if necessary and identify by block number) <table border="0"> <tr> <td>solid state devices</td> <td>surface-wave technology</td> <td>imaging arrays</td> </tr> <tr> <td>quantum electronics</td> <td>photodiode devices</td> <td>infrared imaging</td> </tr> <tr> <td>materials research</td> <td>lasers</td> <td>surface-wave transducers</td> </tr> <tr> <td>microelectronics</td> <td>laser spectroscopy</td> <td></td> </tr> </table>			solid state devices	surface-wave technology	imaging arrays	quantum electronics	photodiode devices	infrared imaging	materials research	lasers	surface-wave transducers	microelectronics	laser spectroscopy	
solid state devices	surface-wave technology	imaging arrays												
quantum electronics	photodiode devices	infrared imaging												
materials research	lasers	surface-wave transducers												
microelectronics	laser spectroscopy													
20. ABSTRACT (Continue on reverse side if necessary and identify by block number) <p>This report covers in detail the solid state research work of the Solid State Division at Lincoln Laboratory for the period 1 May through 31 July 1978. The topics covered are Solid State Device Research, Quantum Electronics, Materials Research, Microelectronics, and Surface-Wave Technology. Funding is primarily provided by the Air Force, with additional support provided by the Army, ARPA, NSF, and DOE.</p>														

DD FORM 1 JAN 73 1473 EDITION OF 1 NOV 65 IS OBSOLETE

UNCLASSIFIED

SECURITY CLASSIFICATION OF THIS PAGE (When Data Entered)

207650

LB